

32 fuses, passive energy dissipation devices, self-centering braces, among others (*e.g.*, Garlock *et al* 2007; Kim and
33 Christopoulos 2008; Vasdravellis *et al* 2013; Dimopoulos *et al* 2016; Tzimas *et al* 2016; Dimopoulos *et al* 2019;
34 Blomgren *et al* 2019; Symans *et al* 2008; Akcelyan *et al* 2016; Freddi *et al* 2013; Gioiella *et al* 2018). These
35 earthquake-resilient steel frame typologies have been extensively studied during the last decade, however, further
36 studies are needed to improve the behavior of their column bases.

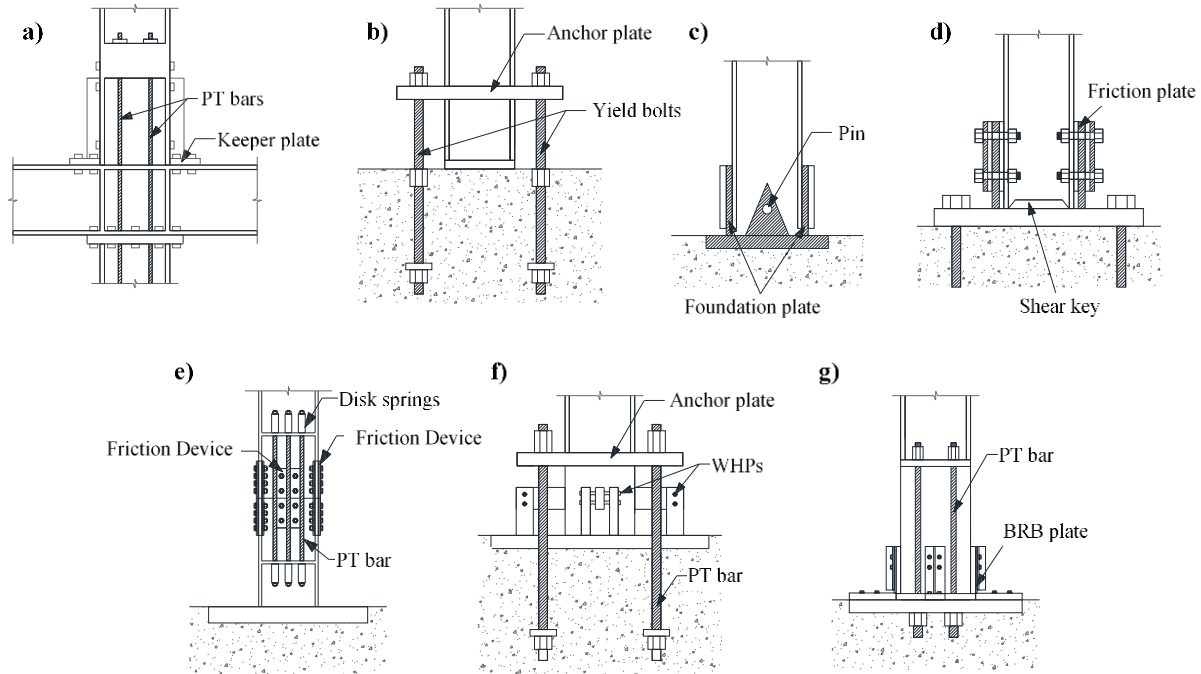
37 Based on the capacity design philosophy of Eurocode 8 (2005) (EN 1998-1-1 2005), conventional steel column
38 bases can be designed as full- or partial-strength joints. In the first approach, plastic hinges are developed in the bottom
39 end of the first story columns, while in the second, the column bases are designed to dissipate energy through inelastic
40 deformations in their main components (*i.e.*, base plates, anchor rods) (EN 1998-1-1 2005; EN 1993-1-8 2005). The
41 design of full-strength joints leads to very strong column bases due to the over-strength factors that account for
42 material variability (Latour and Rizzano 2013) and to conservative foundation designs because the full moment
43 resistance of the column profile is transferred to the foundation. On the other hand, the design of partial-strength joints
44 allows better control of the dimensions of the column bases but requires knowledge of its complex hysteretic behavior
45 under cyclic loading, which is difficult to predict and is affected by strength and stiffness degradation (Latour and
46 Rizzano 2013; Rodas *et al* 2016). Most importantly, for both approaches, field observations after strong earthquakes
47 have confirmed the susceptibility of column bases to difficult-to-repair damage and residual deformations related to
48 concrete crushing, weld fracture, anchor rod fracture, and base plate yielding (Grauvilardell *et al* 2006). In design
49 practice, column bases are assumed to behave as a fully fixed or pinned connection and such assumption may either
50 underestimate or overestimate the story drifts and internal member forces, thus leading to uneconomical or
51 unconservative designs (Zareian and Kanvinde 2013; Kanvinde *et al* 2012).

52 A number of research efforts have proposed alternative solutions with the goal of overcoming the shortcomings of
53 conventional column bases (*e.g.*, Kelly and Tsztoo 1977; Ikenaga *et al* 2006; Mackinven *et al* 2007; Chou and Chen
54 2011; Chi and Liu 2012; Yamanishi *et al* 2012; Takamatsu and Tamai 2005; Grigorian *et al* 1993; MacRae *et al* 2009;
55 Borzouie *et al* 2015; Latour *et al* 2019; Kamperidis *et al* 2018; Wang *et al* 2019; Freddi *et al* 2017). Among the first
56 attempts to develop minimal-damage column bases, Kelly and Tsztoo (1977), proposed and experimentally
57 investigated a partial isolation system associated with an energy-absorbing device that could be easily replaced after
58 an earthquake. The results of this study demonstrated the advantages of damage-free structural systems and promoted
59 many successive studies in this direction.

60 Some of these research works (*e.g.*, Ikenaga *et al* 2006; Mackinven *et al* 2007; Chou and Chen 2011; Chi and Liu

61 2012; Yamanishi *et al* 2012; Takamatsu and Tamai 2005), have focused on the use of rocking column bases where
62 post-tensioned (PT) bars, or yielding bolts, were used to control rocking behavior and to provide self-centering
63 capability, while dedicated devices were used to dissipate seismic energy. Several different configurations were
64 investigated considering different column sections, different lengths and different positions of the PT bars. Two
65 examples of these column bases, respectively by Chi and Liu (2012) and by Yamanishi *et al* (2012) are illustrated in
66 Fig. 1(a) and (b). While in some cases the results showed the advantages of the system in terms of improved self-
67 centering behavior of the column base, several drawbacks were also highlighted including undesirable column axial
68 shortening, loss of post-tensioning force and inelastic deformations. Alternatively, based on the concept of beam-to-
69 column connections with friction devices (FDs), originally pioneered by Grigorian and Popov (1993), other authors
70 further extended this idea to column bases. MacRae *et al* (2009) and Borzouie *et al* (2015) developed two different
71 configurations of column base where the moment resistance and the energy dissipation were provided by friction
72 resistance activated by the relative movement of the column flanges with respect to foundation flange plates with
73 slotted holes. These configurations, respectively illustrated in Fig. 1(c) and (d), allowed to achieve superior behavior
74 under loading in the column strong-axis direction, while damage and stiffness degradation was observed under loading
75 of the column in the weak-axis direction.

76 Recently, Latour *et al* (2019) developed a self-centering base plate connection where FDs were coupled with pre-
77 loaded threaded bars and disk springs as illustrated in Fig. 1(e). The experimental results demonstrated that the system
78 was able to provide energy dissipation and self-centering capabilities along with damage-free behavior. In addition,
79 Kamperidis *et al* (2018) and Wang *et al* (2019) studied two types of low-damage self-centering steel column base
80 connections illustrated respectively in Fig. 1(f) and (g). In both cases, the column base was composed by a concrete-
81 filled square steel section and used external PT strands to control rocking behavior. Two different types of yielding
82 devices, respectively hourglass shape steel yielding devices and sandwiched energy dissipaters, were used to dissipate
83 the seismic energy. Both the numerical simulations and the experimental results demonstrated self-centering behavior
84 and stable energy dissipation of both column base connections demonstrating low residual drifts. However, all the
85 configurations investigated and described so far, do not prevent high stress concentration and damage at the onset of
86 rocking. In addition, they do not provide solutions to control the response of the column base in different plan
87 directions except from the principal direction of the column cross-section.



88
 89
 90 **Fig. 1.** Novel CBs proposed by: (a) Chi and Liu (2012); (b) Yamanishi *et al* (2012); (c) MacRae *et al* (2009); (d)
 91 Borzouie *et al* (2015); (e) Latour *et al* (2019); (f) Kamperidis *et al* (2018); (g) Wang *et al* (2019).

92
 93 In 2017, Freddi *et al* (2017) proposed and numerically investigated a rocking damage-free steel column base, that
 94 can be employed to reduce residual deformations and damage in ‘innovative’ MRFs. The proposed column base,
 95 similarly to previous studies, used PT high-strength steel bars to control the rocking behavior while FDs were used to
 96 dissipate the seismic energy. Amongst others, the main advances with respect to other studies, relates to the circular
 97 steel plate with rounded edges which is used as rocking base. The rounded edges prevent stress concentration and
 98 damage of the contact surfaces while rocking, while the circular shape allows rocking in all plan directions. Freddi *et*
 99 *al* (2017) provided simple analytical equations to describe both the monotonic and cyclic moment–rotation behavior
 100 considering also the possible limit states. These allowed the definition of a design procedure based on non-dimensional
 101 parameters and a simple graphical tool. Both the analytical moment–rotation equations and the design procedure were
 102 validated with the aid of 3D nonlinear finite element (FE) simulations in ABAQUS (2013) that allowed also to evaluate
 103 the local behavior of the components. On the other side, a simplified 2D model of the rocking column base was also
 104 developed in OpenSees (2006) (McKenna *et al* 2006) to assess the influence of the proposed column base on the
 105 global behavior of a structural system. The OpenSees model was used to conduct nonlinear dynamic analyses on a
 106 five-story, five-bay by three-bay steel SC-MRFs with the conventional and proposed rocking column base. The results

107 showed that the proposed rocking column base can fully protect the first story columns from yielding and eliminates
108 the first story residual drift without detrimental effects on peak inter-story drifts.

109 The present paper experimentally evaluates a 3/5 scaled specimen of the rocking damage-free steel column base
110 proposed in Freddi *et al* (2017) under monotonic and cyclic quasi-static loads. The experimental campaign included
111 tests for the characterization of the FDs, required for the definition of important parameters, such as the friction
112 coefficient of the sliding materials and coupon tests for the characterization of the materials. The experimental results
113 demonstrated the damage-free behavior of the column base up to the target design rotation and the ability to limit
114 damage only to few easily replaceable components even under large rotations. The experimental results were also
115 compared and used to calibrate FE models in ABAQUS that will allow further numerical investigations.

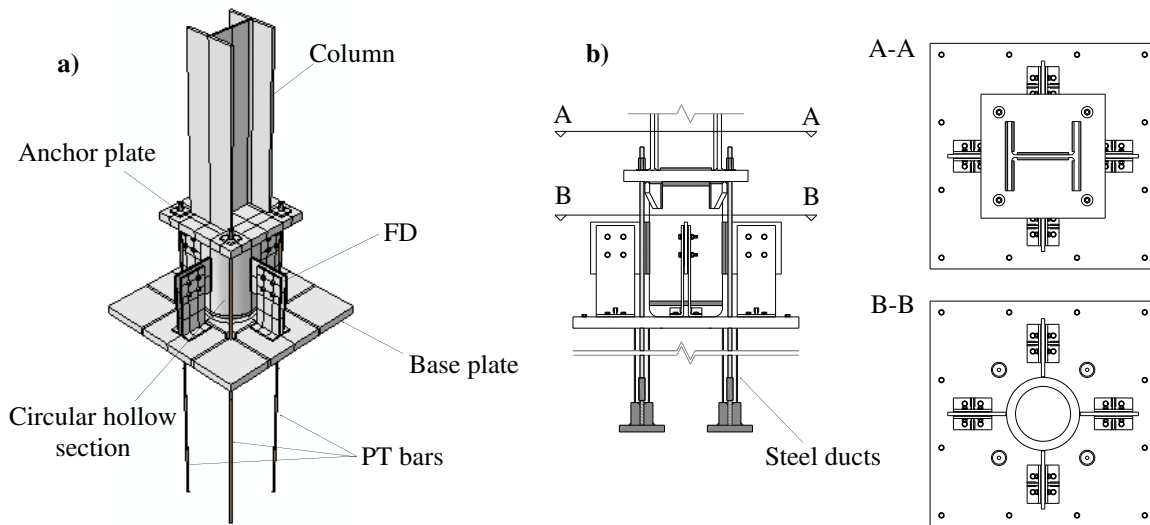
116 **2. ROCKING DAMAGE-FREE STEEL COLUMN BASE**

117 *2.1 Structural details*

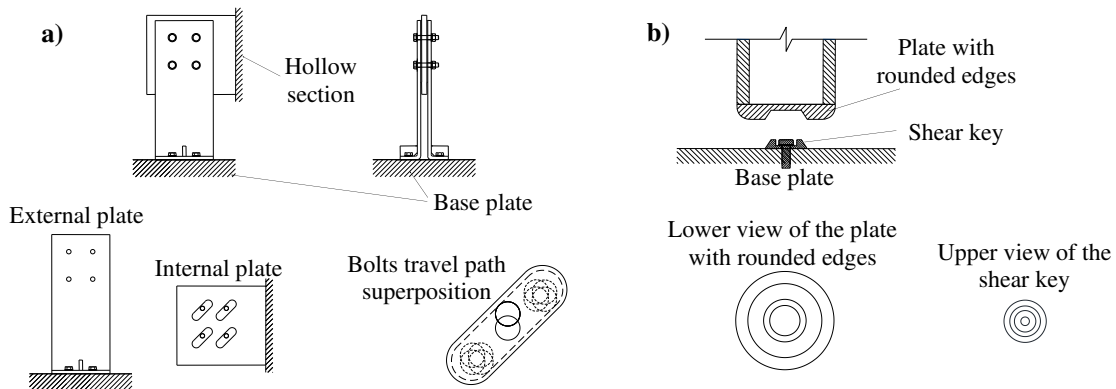
118 Fig. 2 shows the column base proposed and numerically evaluated by Freddi *et al* (2017). A thick steel plate with
119 rounded edges is welded to the bottom of a circular hollow steel section. The rounded edges help the column base to
120 avoid stress concentrations and damage while rocking. Four PT high strength steel bars (or alternatively strands) are
121 symmetrically placed around the center of the column base to increase the axial force in the column and further control
122 the rocking behavior. The PT bars are anchored to the bottom of the foundation (by running them through steel ducts)
123 and to a thick plate welded on the top of the hollow steel section (see the anchor plate in Fig. 2(a)). FDs are placed on
124 the four sides of the column base to provide energy dissipation during rocking. As shown in Fig. 3(a), the FDs consist
125 of two external steel plates bolted to the base plate, an internal steel plate welded to the circular hollow section, and
126 two plates of brass material glued to the external plates at the interface between the external and internal plates.
127 Rocking of the column base results in sliding of the internal plate with respect to the brass and external plates, and
128 thus, dissipates energy through friction. The internal plate is drilled with inclined slotted holes to enable sliding, while
129 the external plates and the brass plates are drilled with aligned rounded holes to accommodate pre-tensioned bolts that
130 are used to tune the friction force in the FDs. The dimensions of the inclined slotted holes are chosen to accommodate
131 the superposition of all possible bolt travel paths during rocking, as shown in Fig. 3(a) (Wolski *et al* 2009). Shear
132 resistance is provided by friction between the base plate and the circular steel section, while as shown in Fig. 3(b), a
133 shear key is included to prevent sliding in case the shear force overcomes the friction resistance. The shear key is
134 designed, such that in the absence of slippage, there is no contact between its coupling parts during rocking.

135 2.2 Moment-rotation behavior

136 Fig. 4(a) shows the dimensions of the column base that control the moment-rotation behavior in the rocking direction,
 137 *i.e.*, b is the dimension of the contact surface; b_{PT} is the distance among the PT bars; b_{FD} is the distance among the
 138 centers of the FDs and h_{FD} is the distance of the centers of the FDs from the base plate. Fig. 4(b) shows the column
 139 base at the onset of rocking with respect to its right edge under the effect of the internal axial force (N), shear force
 140 (V), and bending moment (M). In Fig. 4(b), $F_{PT,u}$ and $F_{PT,d}$ are the forces in the PT bars, while $F_{FD,u}$, $F_{FD,d}$ and $F_{FD,c}$
 141 are the forces in the FDs. The subscripts u and d denote whether the point of application of these forces will move
 142 upwards or downwards during rocking. The subscript c denotes the force in each of the two central FDs. The lever
 143 arms of the forces with respect to the center of rotation $z_{PT,u}$, $z_{PT,d}$, $z_{FD,u}$, $z_{FD,c}$, $z_{FD,d}$ are easily derived from the main
 144 dimensional parameters as discussed in Freddi *et al* (2017).



145 **Fig. 2.** Column base (a) 3D view and (b) lateral view and sections



146 **Fig. 3.** (a) Details of the friction device (FD) and (b) steel plate with rounded edges and shear key

147

148 The moment contribution of the axial force, N , is given by

$$149 \quad M_N = N \cdot \frac{b}{2} \quad (1)$$

150 The forces in each PT bar are function of the rotation, θ , of the column base and are given by

$$151 \quad F_{PT,u} = T_{PT} + K_{PT} \cdot z_{PT,u} \cdot \theta \quad \text{for } \theta \leq \theta_{PT,u,y} \quad (2.a)$$

$$152 \quad F_{PT,d} = T_{PT} - K_{PT} \cdot z_{PT,d} \cdot \theta \quad \text{for } \theta \leq \theta_{PT,d,f} \quad (2.b)$$

153 where T_{PT} is the initial post-tensioning force of each PT bar; $K_{PT} = E_{PT}A_{PT}/L_{PT}$ is the stiffness of each PT bar; E_{PT} , A_{PT}
 154 and L_{PT} are respectively the Young's modulus, the cross-sectional area, and the length of each PT bar; $\theta_{PT,u,y}$ is the
 155 rotation at which the PT bars (in position u) yield; and $\theta_{PT,d,f}$ is the rotation at which the force of the PT bars (in
 156 position d) becomes zero, *i.e.*, when loss of post-tensioning occurs. The PT bars should be designed to avoid either
 157 yielding or loss of post-tensioning for a target rotation θ_T . The moment contribution of the PT bars is given by

$$158 \quad M_{PT}(\theta) = 2 \left[T_{PT} (z_{PT,u} - z_{PT,d}) + K_{PT} (z_{PT,u}^2 + z_{PT,d}^2) \theta \right] \quad \text{for } \theta \leq \theta_T \quad (3)$$

159 The friction force, $F_{FD,i}$, for each friction surface is given by

$$160 \quad F_{FD,i} = \mu_{FD} \cdot n_b \cdot N_b \quad \text{with } i = u, c, d \quad (4)$$

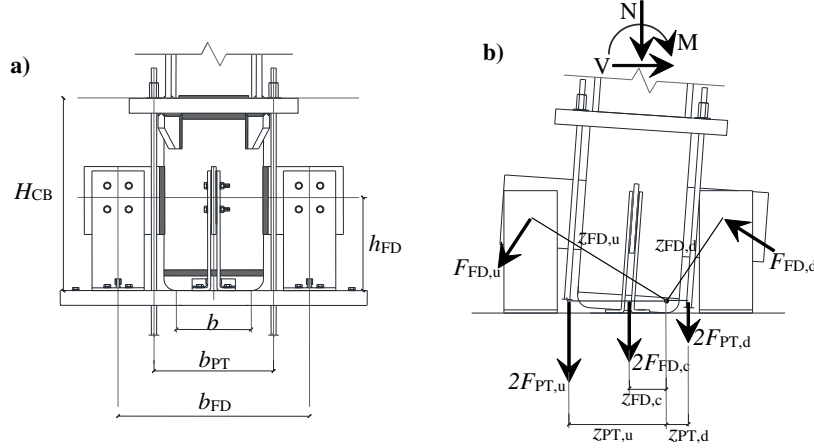
161 where μ_{FD} is the friction coefficient of the surfaces in contact; n_b is the number of bolts and N_b is the bolt pre-loading
 162 force. The moment contribution of the FDs is given by

$$163 \quad M_{FD} = n_{FD} \cdot F_{FD} (z_{FD,u} + 2 \cdot z_{FD,c} + z_{FD,d}) \quad (5)$$

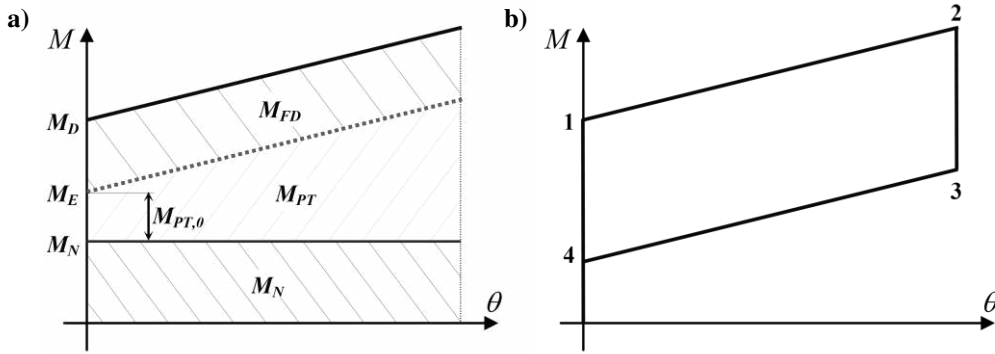
164 Fig. 5(a) shows the moment contributions of the axial force, M_N ; of the PT bars, M_{PT} ; and of the FDs, M_{FD} . The
 165 decompression moment, M_E , and the moment at the onset of rocking, M_D , are given by

$$166 \quad M_E = M_N + M_{PT,0} \quad M_D = M_E + M_{FD} \quad (6)$$

167 where $M_{PT,0}$ is the moment provided by the PT bars at zero rotation, *i.e.*, $\theta = 0.0$ in Eq. (3).



168 **Fig. 4.** Column base (a) fundamental dimensions; (b) forces and lever arms of the friction devices (FDs) and post-
 169 tensioned (PT) bars during rocking for loading from left to right



170 **Fig. 5.** Moment-rotation behavior of the column base. (a) Moment contribution of the axial force, M_N ; of the post-
 171 tensioned (PT) bars, M_{PT} ; and of the friction devices (FDs), M_{FD} and (b) hysteretic behavior
 172

173

174 The rotational stiffness contribution of the PT bars and the moments corresponding to points 1 to 4 of the cyclic
 175 moment-rotation behavior of the column base in Fig. 5(b) are given by

176
$$S_{PT} = 2K_{PT} (z_{PT,u}^2 + z_{PT,d}^2) \quad (7)$$

177
$$M_1 = M_D = M_N + M_{PT,0} + M_{FD} \quad (8.a)$$

178
$$M_2 = M_D + S_{PT}\theta_2 \quad (8.b)$$

179
$$M_3 = M_D + S_{PT}\theta_2 - 2M_{FD} \quad (8.c)$$

180
$$M_4 = M_D - 2M_{FD} \quad (8.d)$$

181 To ensure that the column base provides full self-centering capability, the following relation should be satisfied

182
$$M_4 \geq 0 \quad M_E \geq M_{FD} \quad (9)$$

183 **3. SPECIMEN DESIGN**

184 A column extracted from a building frame was used as case study for the experimental tests. The minimum and
 185 maximum axial forces, N_{Ed} , from the seismic load combination were equal to 510.3 kN and 565.3 kN, respectively.
 186 The axial force from the gravity load of the seismic load combination, $N_{Ed,G}$, was equal to 537.8 kN and was employed
 187 for the design, while the minimum and maximum forces were successively used to assess its adequacy. The cross-
 188 section of the column is a HEB 300.

189 The experimental test was conducted on a 3/5 scaled model (*i.e.*, scaling factor $\lambda = 0.6$) of the prototype column
 190 base. The specimen of the column base was designed based on the dimensions of the scaled column. The scaling factor
 191 $\lambda = 0.6$ was chosen based on the capabilities of the lab and the model scaling was made assuming material scaling
 192 identity. Length units were scaled by λ while areas and forces were scaled by λ^2 . Table 1 contains a comprehensive
 193 list of the similitude scaling factors between the prototype and the test frames.

194 **Table 1.** Similitude scaling factors

Scaling quantity	Units	Dimensional scale requirement	Required scale factor
Stress	S	1	1
Length or Displacement	L	λ	0.6
Area	L^2	λ^2	0.36
Section Moduli	L^3	λ^3	0.216
Moment of Inertia	L^4	λ^4	0.1296
Force	$F=S \times L^2$	λ^2	0.36
Moment	$F \times L = S \times L^3$	λ^3	0.216

195
 196 The column used in the experimental test was a UC 203×203×46, which has similar dimensions with the prototype
 197 column base HEB 300 scaled by λ . The maximum N_{Ed} and $N_{Ed,G}$ scaled by λ^2 are equal to 203.5 kN and 193.6 kN,
 198 respectively. The bending moment resistance $M_{N,Rd}$ evaluated according to the Eurocode 3 (2005) (EN 1993-1-1 2005)
 199 is not influenced by the axial force up to a value N_{Ed} equal to 247 kN, and hence, for the considered case, the bending
 200 moment resistances in the two directions are $M_{N,Rd,y} = 176.58$ kNm and $M_{N,Rd,z} = 81.97$ kNm, respectively. The target
 201 rotation was assumed equal to $\theta_T = 0.03$ rad.

202 Based on the geometry of the column cross-section, the fundamental dimensions of the column base (*i.e.*, b , b_{PT} ,
 203 b_{FD} , and h_{FD}) were selected. A circular hollow section with a 193.7 mm diameter and 30 mm thickness was adopted.
 204 A circular steel plate with the same diameter was welded at the bottom of the hollow section. Standard mechanical

205 processing provided this plate with rounded circular edges having a radius of 30 mm as well as with appropriate space
 206 to accommodate the shear key. The contact surface had a dimension b equal to 143 mm. Due to low availability of PT
 207 bars with small dimensions, 7 wire strands complying with the requirements of the BS 5896: 2012 (2012), were used
 208 in the experiment. The anchor plate of the post-tensioned strands in the top of the hollow steel section was rectangular
 209 and had width, length, and thickness equal to 330 mm, 415 mm and 50 mm, respectively, while the distance between
 210 the strands b_{PT} was equal to 255 mm. The material properties assumed for the design, which are reported in Table 2
 211 (f_y : yield stress; f_u : ultimate stress; E : Young's modulus; β : strain hardening ratio and ν : Poisson's coefficient), were
 212 selected on the basis of experimental results (Coelho *et al* 2004; Haremza *et al* 2013) and on test certificates provided
 213 by the suppliers.

214 **Table 2.** Material properties assumed for the design

Elements		f_y [MPa]	f_u [MPa]	E [GPa]	β	ν
Column and plates	S 355 JR	355	510	210	0.00338	0.30
Post-tensioned strands	BS 5896:2012	1885	1995	195	0.01193	0.30
Bolts	Class 10.9	900	1000	210	0.00855	0.30
Brass	C46400 half hard	200	450	100	0.00839	0.35

215
 216 The design was performed according to the methodology proposed by Freddi *et al* (2017), which is based on the
 217 following Eqs.

$$218 \quad \kappa = \frac{1}{2A_{PT}f_{y,PT}(z_{PT,u} - z_{PT,d})} \left[\frac{M_T - 2 \frac{E_{PT}A_{PT}}{L_{PT}} (z_{PT,u}^2 + z_{PT,d}^2) \theta_T}{1 + \frac{1}{\alpha_{sc}}} - N_{Ed,G} \frac{b}{2} \right] \quad (10)$$

$$219 \quad \kappa \leq 1 - \frac{E_{PT} \cdot z_{PT,u} \cdot \theta_T}{f_{y,PT} \cdot L_{PT}} = \kappa_{max} \quad (11)$$

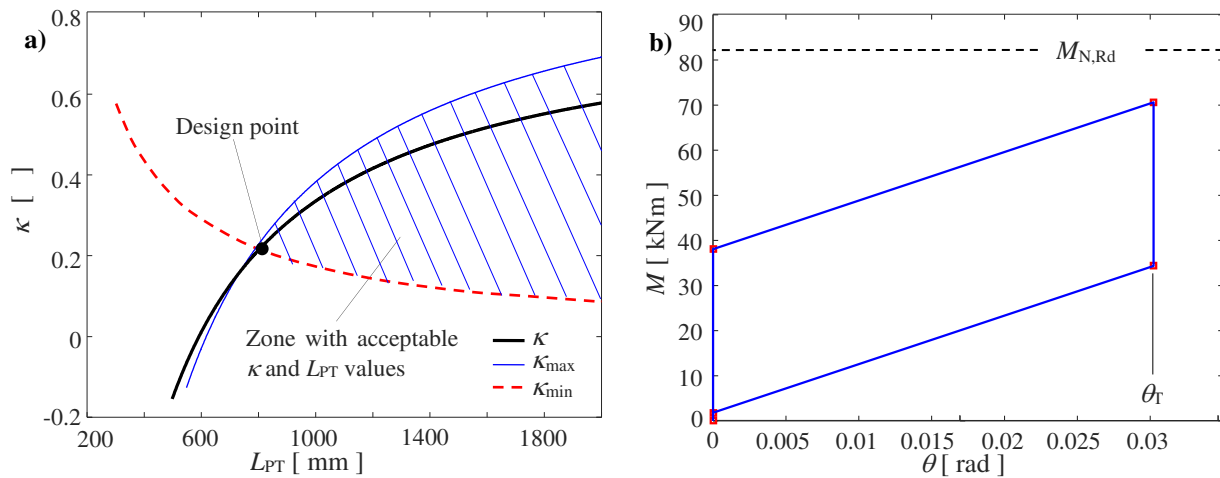
$$220 \quad \kappa \geq \frac{E_{PT} \cdot z_{PT,d} \cdot \theta_T}{f_{y,PT} \cdot L_{PT}} = \kappa_{min} \quad (12)$$

221 where $M_T = M_{N,Rd}/\gamma_T$ is the moment at the target rotation that through the safety coefficient γ_T protects the column
 222 from yielding, while $\alpha_{sc} = M_E/M_{FD}$ is a design parameter that control the self-centering capabilities of the column. A_{PT} ,
 223 L_{PT} and κ are the design variables of the problem and are respectively the area, the length, and the stress ratio of the
 224 post-tensioned strands (*i.e.*, $\kappa = \sigma_{PT}/f_{y,PT}$ where σ_{PT} and $f_{y,PT}$ are respectively the stress and the yield stress of the
 225 strands) that allows definition of the value of the initial post-tensioning force. Once the area of the PT strands, A_{PT} , is

226 selected, Eq. (10) is used to define the initial stress ratio of the post-tensioning strands, κ , as well as their length, L_{PT} ,
 227 in order to meet the design requirements, *i.e.*, to limit the maximum moment at the design rotation θ_T and to provide
 228 self-centering capability. At the same time, Eqs. (11) and (12) constrain the range of values for κ and L_{PT} such that the
 229 limit states defined for the strands, *i.e.*, yielding (corresponding to κ_{max}) and loss of post-tensioning force
 230 (corresponding to κ_{min}) in the strands, are reached for rotations equal, or higher, than the design rotations θ_T . More
 231 details on the design procedure are provided by Freddi *et al* (2017).

232 Considering 7 wire strands of 9.3 mm with an equivalent area of $A_{PT} = 52 \text{ mm}^2$, Fig. 6(a) shows the variation of κ
 233 with respect to L_{PT} . The coefficients γ_T and α_{sc} were assumed equal to 1.165 and 1.10, respectively. Any pair of κ and
 234 L_{PT} with values within the highlighted ‘acceptable zone’ can be selected. However, the optimum design is the one that
 235 satisfies the design criteria and minimizes the length of the PT bars, and hence, is the one that is graphically identified
 236 by the ‘Design point’ in Fig. 6(a). The design procedure provided an L_{PT} equal to 805 mm and κ equal to 0.2175. The
 237 latter corresponds to a T_{PT} equal to 21.3 kN. In this case, the rotations $\theta_{PT,u,y}$ and $\theta_{PT,d,f}$ are equal to 0.0306 rad and
 238 0.0302 rad, respectively. Fig. 6(b) shows the moment-rotation behavior for the column base gap opening mechanism.
 239 The decompression moment, M_E , the moment at the onset of rocking, M_D , and the moment provided by the FDs, M_{FD} ,
 240 are equal to 19.94 kNm, 38.07 kNm and 18.13 kNm, respectively. Fig. 6(b) shows also the bending moment resistance
 241 of the upper column, $M_{N,Rd}$, which is higher than the moment of the column base connection corresponding to the
 242 design rotation θ_T .

243

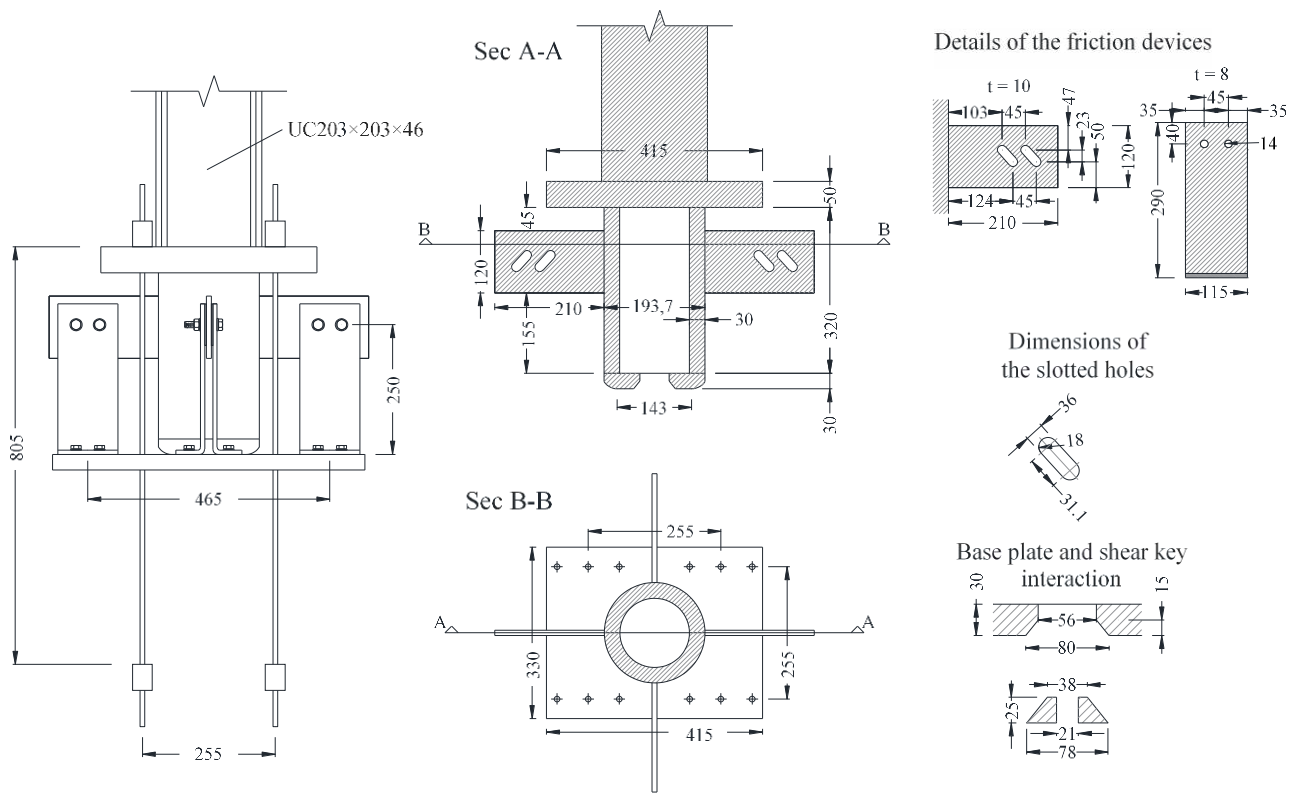


244 **Fig. 6.** (a) Variation of κ with respect to L_{PT} for $A_{PT} = 52 \text{ mm}^2$ and (b) moment-rotation behavior of the column base

245

246 Once the strands were designed, M_{FD} was derived by M_E and α_{sc} and then the FDs could be designed by selecting
 247 appropriate values of the parameters in Eq.s (4) and (5). FDs were introduced on the four sides of the column base,
 248 and the relevant dimensions were $b_{FD} = 465$ mm and $h_{FD} = 250$ mm. Hence, the required friction force in each friction
 249 surface of the four FDs obtained by Eq. (5) was $F_{FD} = 10.87$ kN. The thickness of the internal and external plates of
 250 the FDs were 10 mm and 8 mm, respectively. Two 3 mm thick brass plates were used as friction interfaces, and two
 251 M12 class 10.9 bolts were used to apply the pre-loading force by tightening. The friction coefficient at the brass-steel
 252 interface was evaluated by preliminary tests described in Section 5. Successively, the pre-loading force was defined
 253 based on the friction coefficient to achieve the required friction force. The dimensions of the slotted holes were
 254 designed to allow a rotation larger than the target rotation θ_T without bearing of the bolts on the plates (*i.e.*, about 0.06
 255 rad). Fig. 7 summarizes the geometry of the column base.

256



257
 258 **Fig. 7.** Geometry of the specimen (dimensions in mm)

259

260 **4. INSTRUMENTATION**

261 Amongst others, hydraulic jacks, load cells, linear variable differential transformer (LVDT), strain gauges and a torque

262 wrench have been used during the tests. Specifications of the hydraulic jacks and load cells are listed in Table 3 and
 263 Table 4. 10 mm linear strain gauges with mild steel compensation have been employed, while the Norbar PRO 100
 264 1/2" torque wrench with a min and max torque of 20 and 100 Nm has been used to control the tightening of the bolts.
 265 In addition, the universal testing machine DARTEC 9500 have been used for the characterization tests of the FDs and
 266 for the coupon tests of the steel materials. Data acquisition and tests management have been performed in LabView.

267 **Table 3.** Hydraulic jacks employed in the tests

Actuators	Acronym	Use	Max force [kN]	Stroke [mm]	Weight [kg]
Servocon System		Application of the horizontal force	±250	±150	
Hi-Force HHS102	HJA	Post-tensioning of strands	+110	+50	3
Yale YCS 57-70	HJB	Post-tensioning of PT bars	+567	+70	25

268 **Table 4.** Load cells employed in the tests

Load Cells	Acronym	Measuring	Max force [kN]
Novatech F207	LCA	Axial force in the bolts of the FDs	+80
Novatech F313	LCB	Axial force in the 7 wire strands (9.3 mm)	+200
Novatech F203	LCC	Axial force in the PT bars (15 mm)	+600

269

270 5. CHARACTERIZATION OF THE FRICTION DEVICES

271 The friction force, $F_{FD,i}$, of each friction surface is given by Eq. (4) and is affected by the bolts pre-loading force, N_b ,
 272 and the friction coefficient of the brass-steel interface, μ_{FD} . The preliminary tests described in this section allowed to
 273 characterize the FDs parameters to gain confidence in: *i*) the definition of the bolts pre-loading force, N_b , used in the
 274 tests and *ii*) the definition of the friction coefficient, μ_{FD} , for the interface materials.

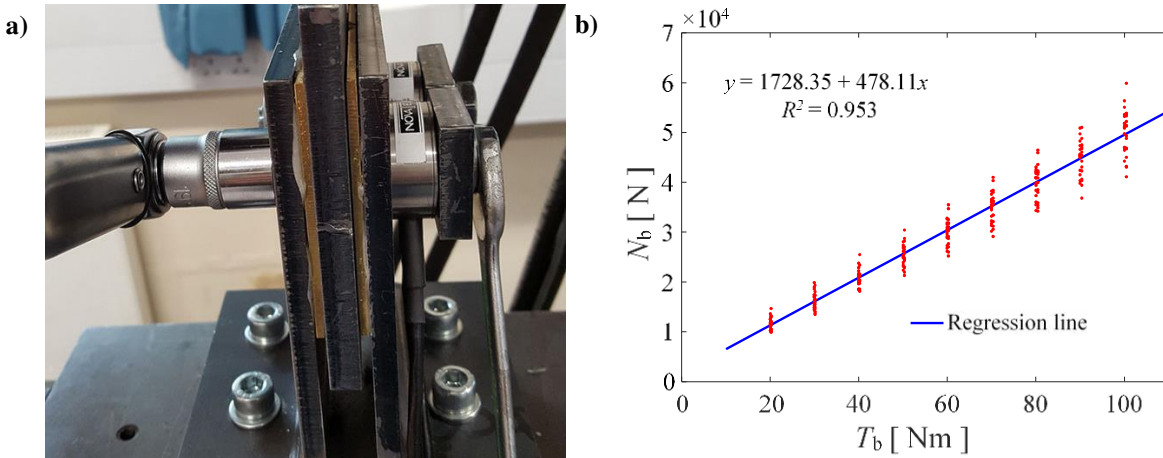
275 5.1 Relationship between torque and the bolt pre-loading force

276 The bolts pre-loading force can be determined from the tightening torque by the following equation

$$277 N_b = \frac{T_b}{\alpha \cdot d} \quad (13)$$

278 where T_b is the value of the tightening torque, d is the bolt diameter, and the recommended value of α is equal to 0.2
 279 (Latour *et al* 2015). It was observed by previous studies that this relationship may under- or over-estimate the bolt
 280 pre-loading force, N_b , by 20% due to different bolt type and differences in temperature, humidity, thread conditions,
 281 lubrication, etc. Hence, the characterization tests aimed at deriving the α parameter that best described the relationship
 282 between the tightening torque T_b and bolt pre-loading force, N_b , for the M12 bolts Class 10.9 used in the tests.

283 Characterization tests were performed considering 30 bolts with 9 different torque values from 20 Nm to 100 Nm.
 284 The tightening torques were applied by a Norbar torque wrench, while the bolt's pre-loading force was measured with
 285 load cells (LCA in Table 4). Fig. 8(a) shows the test setup, while Fig. 8(b) shows the experimental results. Regression
 286 of a total of 270 samples provided a value for α equal to 0.1743.



287 **Fig. 8.** Characterization test for the friction devices (FDs). Relationship between the tightening torque T_b and the bolt
 288 pre-loading force N_b . (a) Representation of the tests' setup; (b) test results and interpolation curve

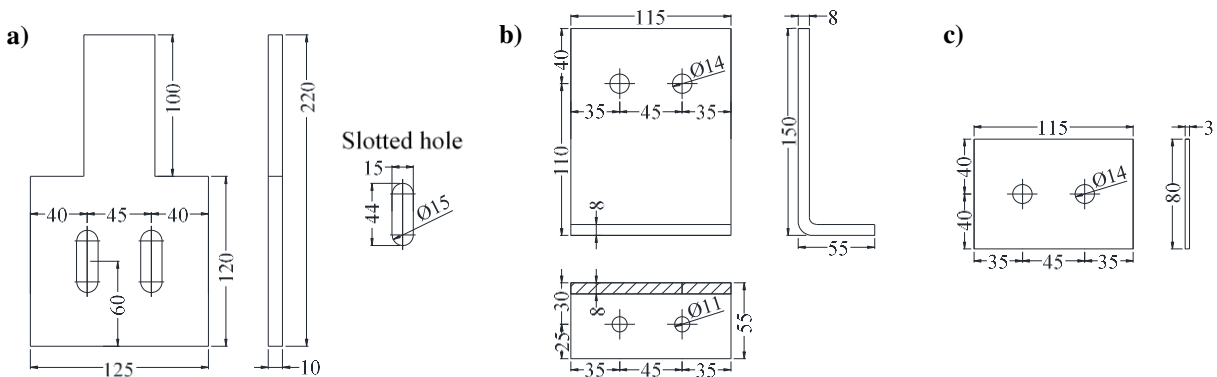
289

290 5.2 Tests for the friction coefficient of the materials interface

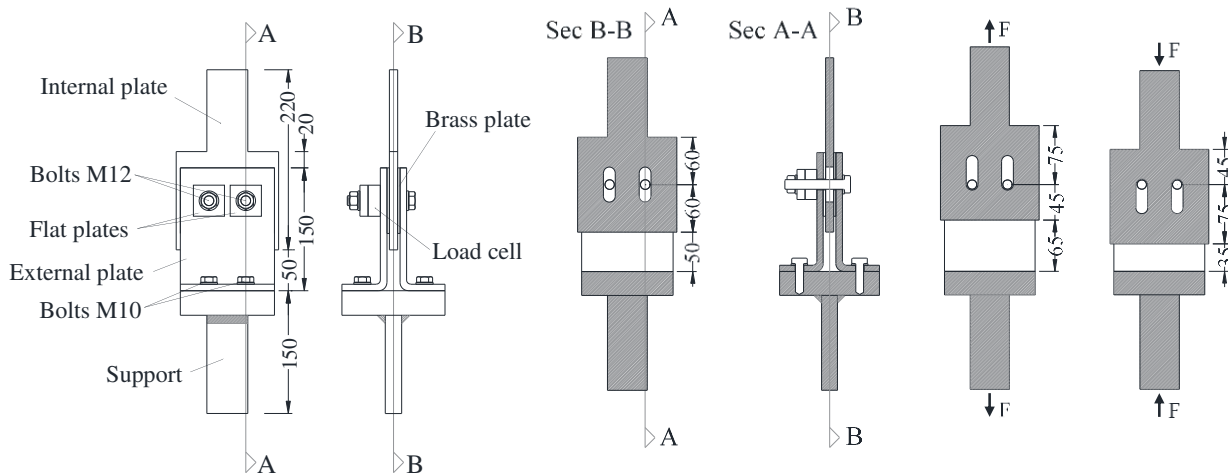
291 This part of the study provided the static and kinetic friction coefficient of the brass-steel interface, μ_{FD} , allowing also
 292 the evaluation of its variability during the cyclic displacement histories. To allow for relative displacements between
 293 the plates in the friction surfaces and to accommodate the travel path of the bolts, the inner plate of the FD, had slotted
 294 holes with dimensions of 44 by 15 mm as shown in Fig. 9(a). The two outer steel plates and the inner brass friction
 295 plates in Fig. 9(b) and (c) had circular holes and were glued together with Araldite Epoxy Adhesive. The clamping
 296 force was applied by two M12 bolts 10.9 class and the holes were of 14 mm, leaving extra tolerance with respect to
 297 the recommendations of the Eurocode 3 (EN 1993-1-8 2005). The dimensions of the friction surfaces were the same
 298 as for the FDs used in the tests of the column base. The brass material was 'C46400 half hard', while the material used
 299 for the steel components was S355.

300 Quasi-static tests were performed using the configuration showed in Fig. 10 and were carried out under 20 loading
 301 cycles with a linear variation of the displacement, a constant amplitude of ± 10 mm, and a frequency equal to 0.25 Hz
 302 as shown in Fig. 12. Fig. 11(a) shows two instants during the test that correspond to the maximum and minimum
 303 displacements, while Fig. 11(b) and (c) show, respectively, the internal plate with slotted holes and one brass plate
 304 after the test. Four tests were conducted for different levels of pre-loading force, *i.e.*, starting from 10 kN up to 25 kN,

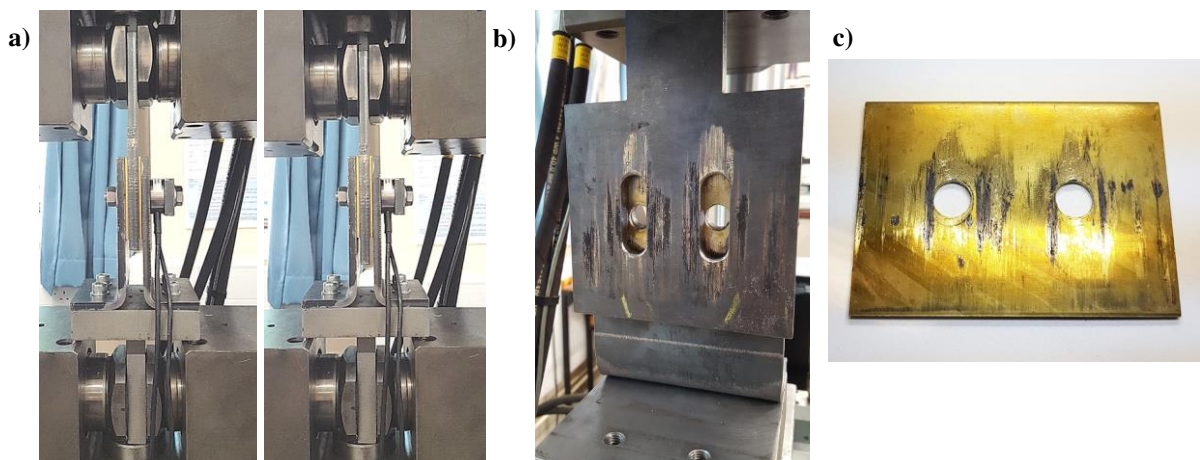
305 with an increment of 5 kN at each step. The initial pre-loading force in the bolts, N_b , and its variation during the tests
 306 was monitored with load cells (LCA in Table 4).



307 **Fig. 9.** Characterization test for the friction devices (FDs). Friction coefficient. (a) Internal plate with slotted holes;
 308 (b) external plate and (c) brass plate (dimensions in mm)



309 **Fig. 10.** Characterization test for the friction devices (FDs). Friction coefficient. Dimensions under the maximum and
 310 minimum displacement configuration (dimensions in mm)



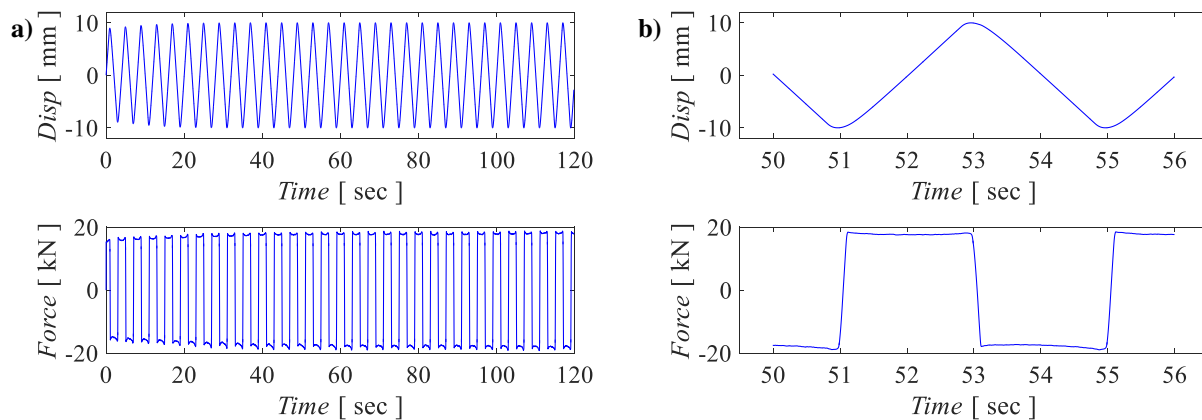
311 **Fig. 11.** Characterization test for the friction devices (FDs). Friction coefficient. (a) Front view with maximum and
 312 minimum displacements of the friction device (FD); (b) internal plate with slotted holes and (c) brass plate with
 313 circular holes after the test

314 The friction coefficient was determined by

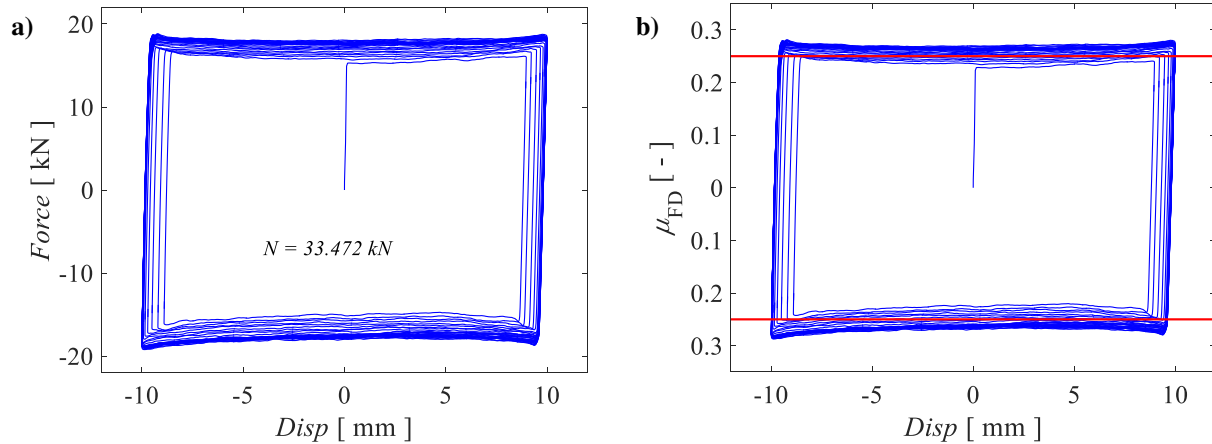
315
$$\mu_{FD} = \frac{F_{FD}}{m \cdot n \cdot N_b} \quad (14)$$

316 where $m = 2$ is the number of surfaces in contact, $n = 2$ is the number of bolts, N_b is the bolt pre-loading force while
317 F_{FD} is the sliding force. The results of Fig. 12 and Fig. 13 refer to the test with the bolts' pre-loading force equal to 15
318 kN. Fig. 12(a) shows the displacement and force history, respectively, for the whole duration of the test, while Fig.
319 12(b) shows the results for the cycle from 50 to 56 seconds. Fig. 13(a) shows the force-displacement response that,
320 considering the average normal force acting on the friction interface during the whole load history, which is equal to
321 33.47 kN, allowed to derive Fig. 13(b) which shows the friction coefficient according to Eq. (14).

322 Fig. 13(a) shows the force-displacement behavior exhibiting a slight kinematic hardening similarly to what was
323 observed by Latour *et al* (2015). This is due to the changes in the contact surfaces, which were initially smooth. During
324 sliding motion, the number of asperities increased due to the high contact pressures and to the wearing of the brass,
325 causing an increase in interlocking friction components in the final surface, as shown in Fig. 11(b) and (c). Fig. 13(a)
326 shows an increase of the friction coefficient that, after a few cycles, become stable with an increased sliding force of
327 the order of 10 % with respect to the force corresponding to the first sliding. Consistent results were obtained for the
328 other pre-loading forces and the average value of the friction coefficient, μ_{FD} , was equal to 0.25. It is important to
329 highlight that for the pre-loading force of 25 kN, debonding of the external plate with the interface plate was observed.
330 For this reason, a limited value of the bolts pre-loading force was used in the full-test of the column base as described
331 in Section 7.



332 **Fig. 12.** Characterization test for the friction devices (FDs). Displacement and force history of the friction device (FD)
333 test with pre-loading force in each bolt of 15 kN



334 **Fig. 13.** Characterization test for the friction devices (FDs). Initial pre-loading force in each bolt of 15kN. (a) Force–
 335 displacement hysteretic curve and (b) normalized force for the definition of the friction coefficient μ_{FD}

336

337 6. COUPON TESTS

338 The elements experiencing stresses beyond their yield stress (for rotations larger than the θ_f) included the post-
 339 tensioned strands and the FDs. Certificates for the strands' stress-strain behavior were available from the supplier. For
 340 the characterization of the material properties of the plates of the FDs, coupon tests were performed using of the
 341 universal testing machine DARTEC 9500. Three coupon specimens for the FDs' plates were subjected to tensile tests
 342 according to the EN ISO 6892-1 (2009). Specimen strains were measured using an axial extensometer. Average values
 343 of the properties of the steel for each component are listed in Table 5.

344 **Table 5.** Steel Properties

Test	Yield Stress [MPa]	Yield Strain [%]	Young Modulus [MPa]	Tensile Strength [MPa]	Maximum Elongation [%]
1	335	0.166	201807	467	31.5
2	327	0.165	198181	452	32.7
3	332	0.164	202439	457	30.2
Average Values	331.3	0.165	200809	458.6	31.47

345

346 7. EXPERIMENTAL TEST ON THE ROCKING COLUMN BASE

347 7.1 Test setup and instrumentation

348 The proposed column base was tested by using the test setup shown in Fig. 14 and illustrated in the photos of Fig. 15.
 349 The test setup was designed based on the space available in the lab and on the strong floor connections that were
 350 placed as a square wire every 406.4 mm.

351 7.2 *PT bars*

352 Two external Dywidag PT bars with diameter of 15 mm ($A_{PT,ext} = 177 \text{ mm}^2$; diameter after thread of 17 mm) and yield
353 and ultimate stresses equal to $f_{y,PT,ext} = 900 \text{ MPa}$ and $f_{u,PT,ext} = 1100 \text{ MPa}$, were used to simulate the axial forces due to
354 gravity loads. The parameters affecting the stiffness of the PT bars were the free length and the Young's modulus,
355 which were equal to $L_{PT,ext} = 1826.9 \text{ mm}$ and $E_{PT,ext} = 205000 \text{ MPa}$. The PT bars were connected at one end to the
356 upper beam, which transfers the force to the column, and at the other end to two anchor supports connected to the
357 strong floor. Hollow hydraulic jacks type B (HJB in Table 3, in Fig. 14 and Fig. 16(a)) were used to apply the post-
358 tensioning force. The load cells type C (LCC 1 and 2 in Table 4, in Fig. 14 and Fig. 16(b)) were used to calibrate the
359 initial force and to measure its variation during the tests. After post-tensioning through the hydraulic jacks,
360 intermediate bolts, as shown in Fig. 16(a), were placed and tightened to the web of the upper beam to avoid loss of
361 PT force as consequence of the loss of pressure in the hydraulic jacks. The design initial PT force for the external bars
362 was equal to 96.3 kN. During the rocking, the uplift of the column base produced an increase of the tension force of
363 the PT bars which was measured during the test.

364 In addition to the axial force imposed by the PT bars, the total force was increased by the weight of all the
365 components of the specimen and of the test setup. The weight of the upper beam and the column were respectively
366 equal to 175 kg and 180 kg, while the total weight was equal to 430 kg. This value does not account for half of the
367 weight of the horizontal actuator and hinges that was equal to 130 kg.

368 7.3 *Steel basement and post-tensioned strands*

369 The column was placed on a steel basement, which included the anchor plates for the strands as shown in Fig. 14, Fig.
370 16(c) and (e). The strands were fixed to the anchor plate of the steel basement from one side, and post-tensioned
371 through hollow hydraulic jacks type A (HJA in Table 3, in Fig. 14 and Fig. 16(g)), which were supported by the anchor
372 plate of the column base on the other side. Similar to the external PT bars, the strands were fixed to the upper anchor
373 plate by the intermediate anchor grips to avoid loss of PT force. This was made possible thanks to the supports shown
374 in Fig. 14 and Fig. 16(g). The design PT force for the strands was equal to 21.3 kN. The anchor grips were composed
375 by wedges coupled with open barrels as showed in Fig. 16(d). Four load cells type B (LCB in Table 4, in Fig. 14 and
376 Fig. 16(e)) were located between the anchor grips and the anchor plates in the steel basement to calibrate the initial
377 post-tensioning force in the strands and to measure force variations during the tests. The upper plate of the steel
378 basement was provided with oversized holes so that the strands were free to move laterally during the column rocking.

379 In addition, the upper plate included threaded holes for the connection of the FDs and the shear key. Fig. 16(c) shows
380 the shear key fixed to the steel basement.

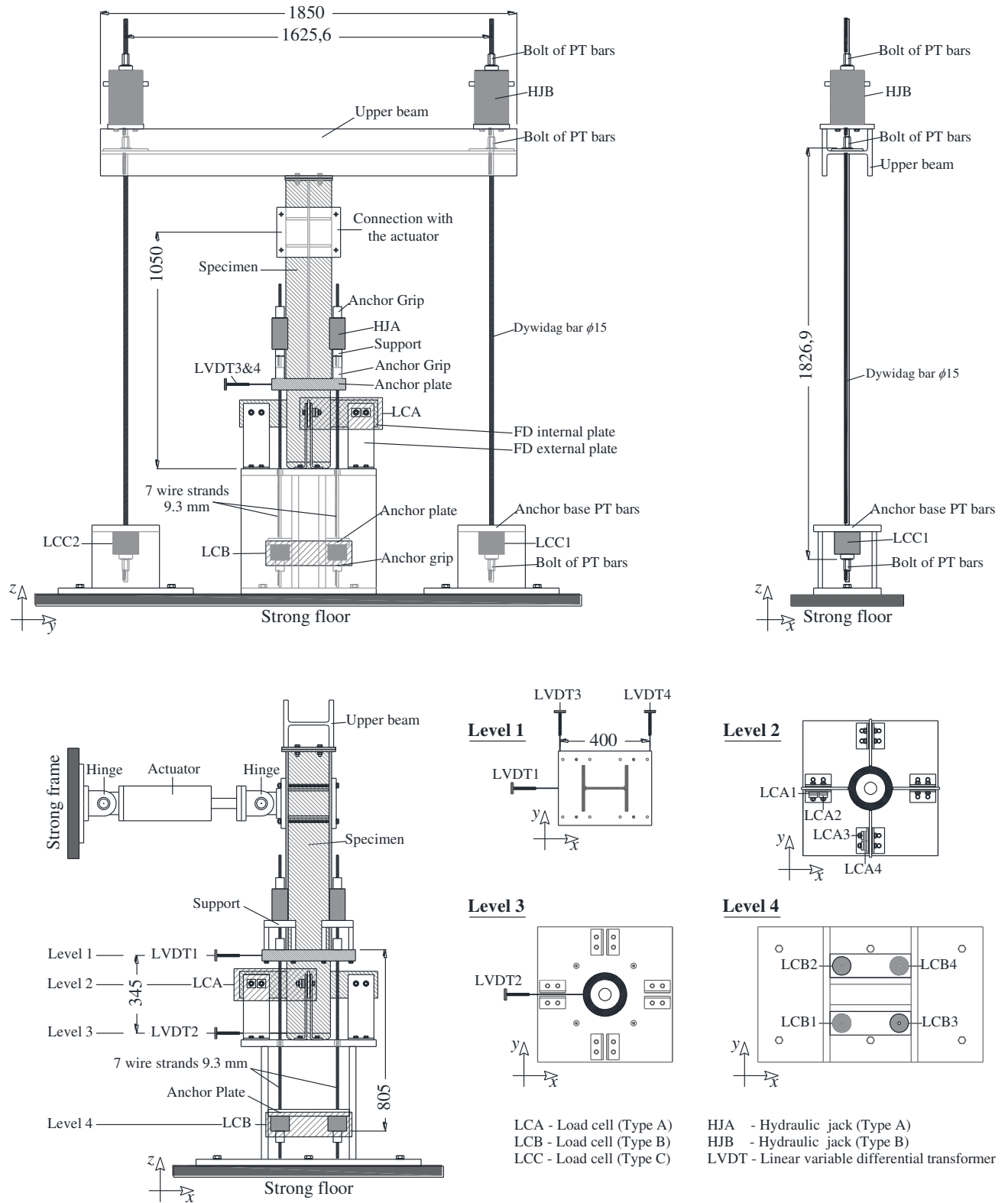
381 *7.4 Friction devices*

382 Each external plate of the FDs was bolted to the steel basement with two M10 bolts. The FDs had the same
383 configuration used in the characterization tests with the only exception that the internal plates had inclined slotted
384 holes to accommodate the bolts travel path. The internal plates were welded to the column as shown in Fig. 16(h) and
385 (i). Four load cells type A (LCA in Table 4, Fig. 14 and Fig. 16(h)) were used to measure the variation of the axial
386 force in four of the eight bolts of the FDs.

387 According to the original design, the bolts' pre-loading force in the friction devices was equal to 21.74 KN. This
388 required a tightening torque equal to $T_b = 45.47$ Nm. However, to avoid the debonding of the brass plates, that was
389 observed in the FDs' characterization tests, and which could jeopardize the full-scale tests, the bolts' pre-loading force
390 was set to 10 kN by applying a tightening torque, T_b , of 20.92 Nm.

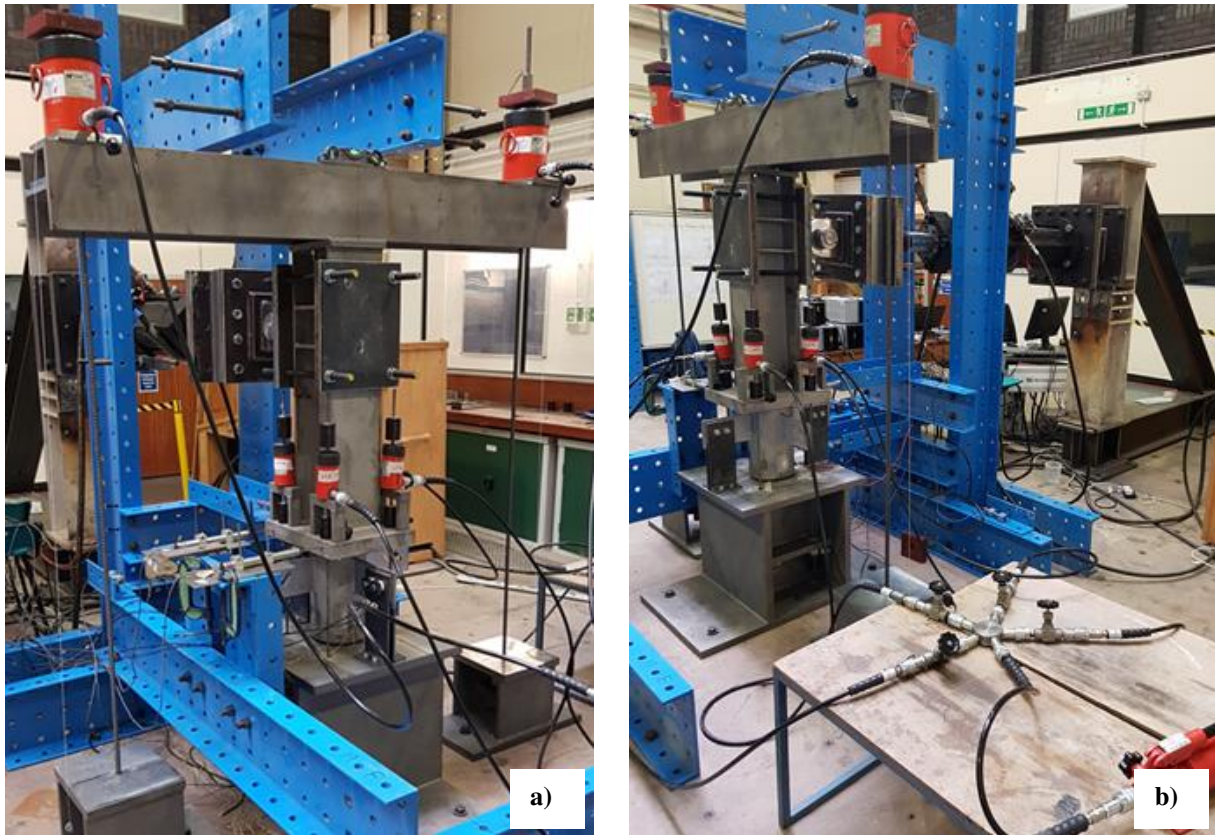
391 *7.5 Other components*

392 LVDTs 1 to 4, as shown in Fig. 14 and Fig. 16(g), were placed in the column base at different heights in order to
393 measure the horizontal translations, rotations in the longitudinal direction, as well as, the horizontal translations in the
394 transverse direction and torsions. Moreover, in order to evaluate the stresses and deformation of the circular hollow
395 cylinder of the column base, two strain gauges at each side, were introduced in the position close to the pivot points
396 of the rocking as shown in Fig. 16(h). Finally, the specimen was connected with the horizontal actuator, which was
397 fixed to a steel strong frame as shown in Fig. 15. The actuator was connected at both the ends by hinges to avoid any
398 transfer of moment to the column.

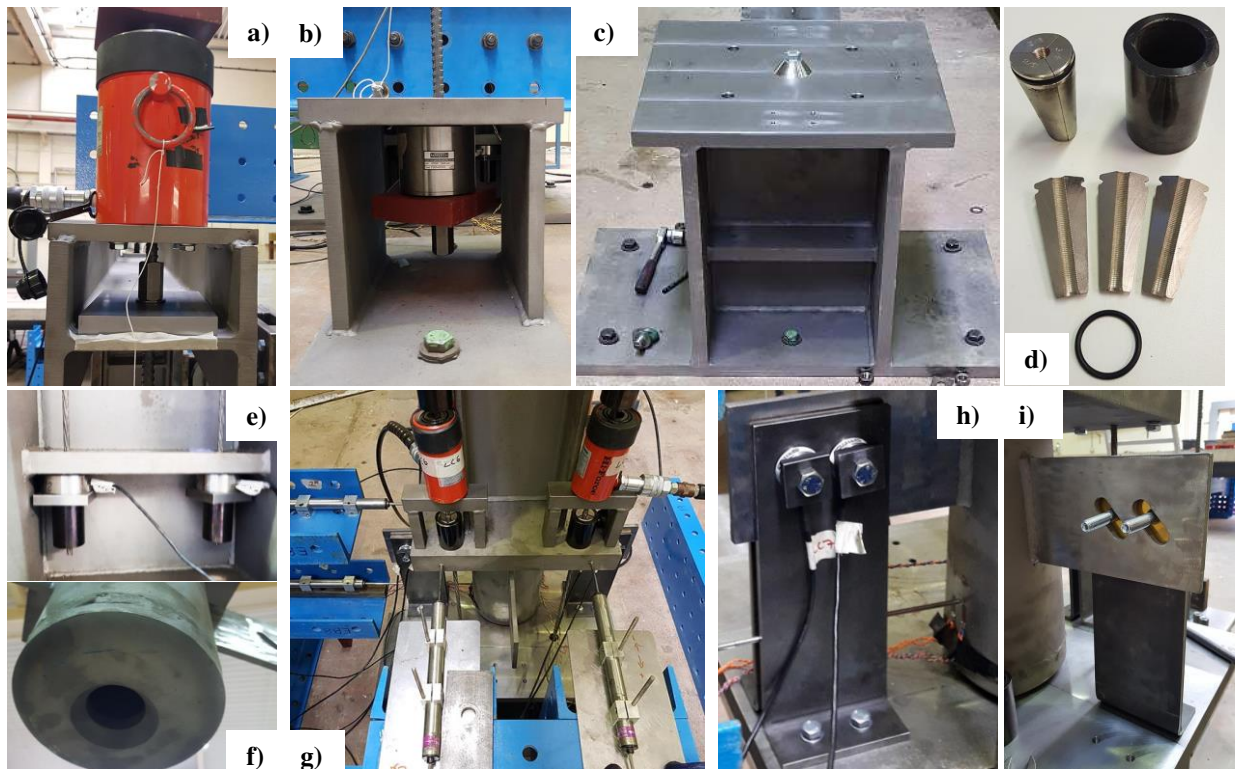


399
400

Fig. 14. Tests Setup and instrumentation (dimensions in mm)



401 **Fig. 15.** Full-test setup



402 **Fig. 16.** Full-test setup components and instrumentation

403

404 **8. EXPERIMENTAL RESULTS**

405 Quasi static cyclic tests were performed for different configurations that included different components of the column
406 base, *i.e.*, PT bars for the axial force only (test type A); PT bars and strands only (test type B); PT bars, strands, and
407 FDs in the longitudinal direction only (test type C); and the complete column base (test type D), as indicated in Table
408 6. This allowed to experimentally decouple the moment contributions from each component. Preliminary tests were
409 performed with different amplitudes without overcoming the elastic behavior of the strands and up to the target design
410 rotation, θ_T . The results of these cyclic tests are shown, for all the tests' configurations, in Fig. 17 and Fig. 18.
411 Additionally, a final test with cyclic displacements of increasing amplitude was conducted showing the damage-free
412 behavior of the column base up to the target design rotation, θ_T while for amplitudes higher than θ_T , yielding of the
413 strands occurred, and the failure of the FDs' plates due to bolts bearing was observed for very large rotations. The
414 results are shown in Fig. 20 and Fig. 21.

415

416 **Table 6.** Tests configurations

Test types	Components included
A	PT bars
B	PT bars and PT strands
C	PT bars, PT strands and longitudinal FDs
D	PT bars, PT strands, longitudinal and transverse FDs

417

418 It is worth mentioning that, while the analytical formulation reported in Sections 2 and 3 considers only the rotation
419 related to the gap opening, the column base rotation observed during the test, and reported in the following part of the
420 paper, was measured based on the relative displacement of the LVDTs 1 and 2 divided by the distance between the
421 two and hence accounts also for the deformability of the test setup. Moreover, it is important to point out the difficulties
422 in applying the exact values of the initial forces in PT bars, strands, and bolts. However, these differences between the
423 designed column base and the one actually tested, do not affect the final outcomes of the experimentation. The applied
424 forces were measured in the experimental tests and FE models were successively adjusted to replicate the forces
425 measured during the tests to evaluate their ability to represent the experimental results. Similarly, the test setup was
426 included in the numerical model to account for its deformability. The numerical models were developed in ABAQUS
427 (2013) and are discussed in Section 9.

428

429 8.1 Preliminary tests

430 Fig. 17 shows the experimental results for the cyclic test of column base type A for rotations up to about 0.045 rads.

431 Fig. 17(a) shows the moment-rotation curve, while Fig. 17(b) shows the tension force variation in the PT bars.

432 Similarly, Fig. 18 shows the experimental results for the cyclic test up to the target rotation ($\theta_T = 0.03$ rads, 3 % drift)

433 for the column base types B, C, and D. Fig. 18(a) shows the moment-rotation curves where it can be observed the

434 elastic behavior of the column base type B and the influence of the FDs in dissipating energy. The small difference

435 between the curves C and D shows the low influence of the transverse FDs as consequence of their small displacement

436 and short lever arm with respect to the pivot point of rocking. However, their presence allows to dissipate the seismic

437 energy when the column is subjected to loads in a different direction. The small residual displacement was related to

438 the imperfections of the coupling of the column base plate with the steel basement, as will be discussed in Section 9.

439 Fig. 18(b) shows the tension in the PT bars and as expected for these components, there is a superposition of the curves

440 for column base types B, C, and D. The same applies for the strands' tension force and the strain gauges' measurements,

441 as such, for simplicity, only the results of the column base type B are shown. Fig. 18(c) shows the tension force

442 variation in the strands. Their initial PT force was equal to 29.65 kN with very small differences from strand to strand.

443 Their behavior was elastic and, the tension force showed different stiffness for negative and positive values of the

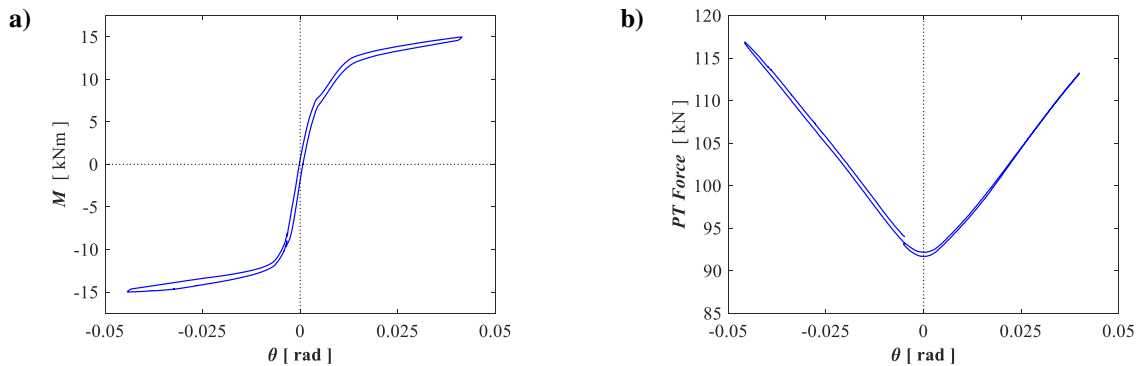
444 rotation due to the change of the pivot point when rocking which results in changes to the length of the lever arm. Fig.

445 18(d) shows the strain gauges measurements. Only strain gauges 1, 2, and 4 are shown since strain gauge 3 was

446 damaged during the test. The results show the compression and decompression of the column edge while rocking,

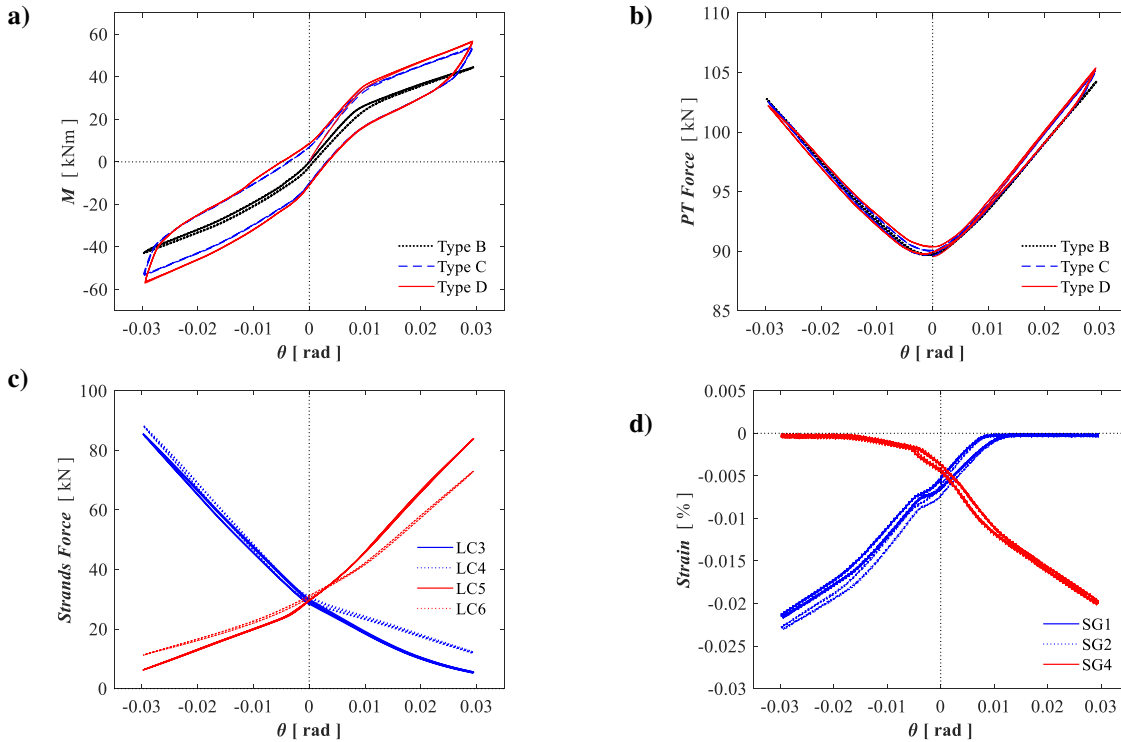
447 demonstrating the elastic behavior of the material.

448



449 **Fig. 17.** Cyclic test of the column base type A. (a) Moment-rotation curve and (b) tension force in the PT bars

450



451 **Fig. 18.** Cyclic test of the column base types B, C and D up to the target rotation. (a) Moment-rotation curve; (b) PT
 452 bars tension force; (c) strands' tension force for the column base type B and (d) strain gauges' records the column
 453 base type B

454

455 **8.2 Final tests**

456 The final test was conducted on the complete column base (type D) with increasing amplitudes up to the first
 457 component's failure by using a loading protocol that complies with the test requirements of AISC 341-16 (2005) for
 458 'link-to-column moment connections'. The load protocol consisted of cyclic lateral displacements with increasing
 459 amplitude imposed in a quasi-static fashion as reported in Table 7. The protocol included three initial sets of six cycles
 460 at 8.25, 11, and 16.5 mm displacements, four subsequent cycles at 22 mm, and five sets of two cycles at 33, 44, 66,
 461 88 and 100 mm. The specimen was also monotonically pushed to a displacement equal to 150 mm to identify the
 462 failure mode. Fig. 19 shows two displacements configurations considering the column at the onset of rocking on the
 463 right and left edges respectively for rotations of 0.095 and 0.143 rads (9.5 % and 14.3 % drift).

464 Fig. 20(a) shows the moment-rotation curves for cycle types from 1 to 5 with displacements amplitudes up to 33
 465 mm (0.0314 rads, 3.14 % drift) while Fig. 20(b) shows the moment-rotation curves for the whole test. Fig. 21 shows
 466 the results for the moment-rotation curves, tension in the PT bars, tension in the strands, measurements from the strain
 467 gauges, and tension force in the bolts independently for the cycle types from 1 to 5, 6 and 7 and from 8 to 10. In this

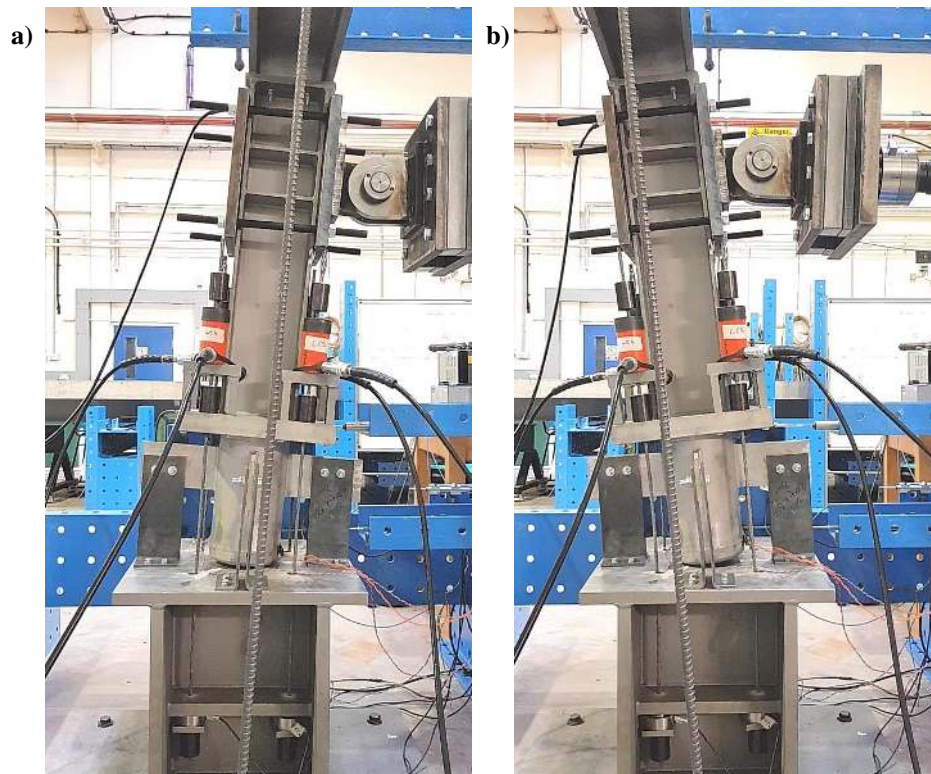
468 figure, together with the cycles in the displacement interval, the dotted black line shows also one cycle before and
 469 after, providing a better representation of the results' variation.

470 The results shown in Fig. 20(a) are similar to what is observed in the preliminary tests and show the elastic and
 471 damage-free behavior of the components up to the target rotation. Additional information provided by this final test
 472 are related to the behavior of the column base for rotations beyond the target one, as shown in Fig. 20(b) and more in
 473 detail in Fig. 21.

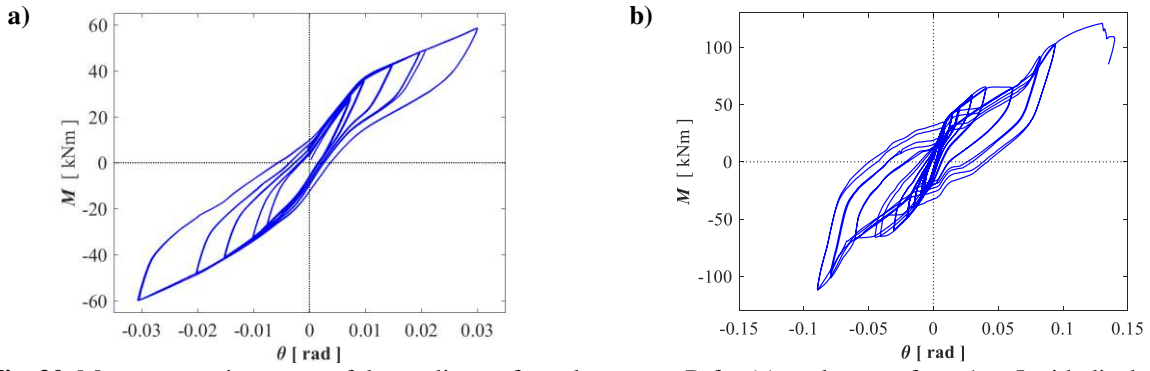
474 **Table 7.** Load protocol

Cycle types	Number of cycles	Amplitude [mm]	Rotation [rad]	Drift [%]
1	6	8.25	0.0078	0.78
2	6	11	0.0105	1.05
3	6	16.5	0.0157	1.57
4	4	22	0.0210	2.10
5	2	33	0.0314	3.14
6	2	44	0.0419	4.19
7	2	66	0.0629	6.29
8	2	88	0.0838	8.38
9	2	100	0.0952	9.52
10	Monotonic up to 150 mm		0.1430	14.3

475

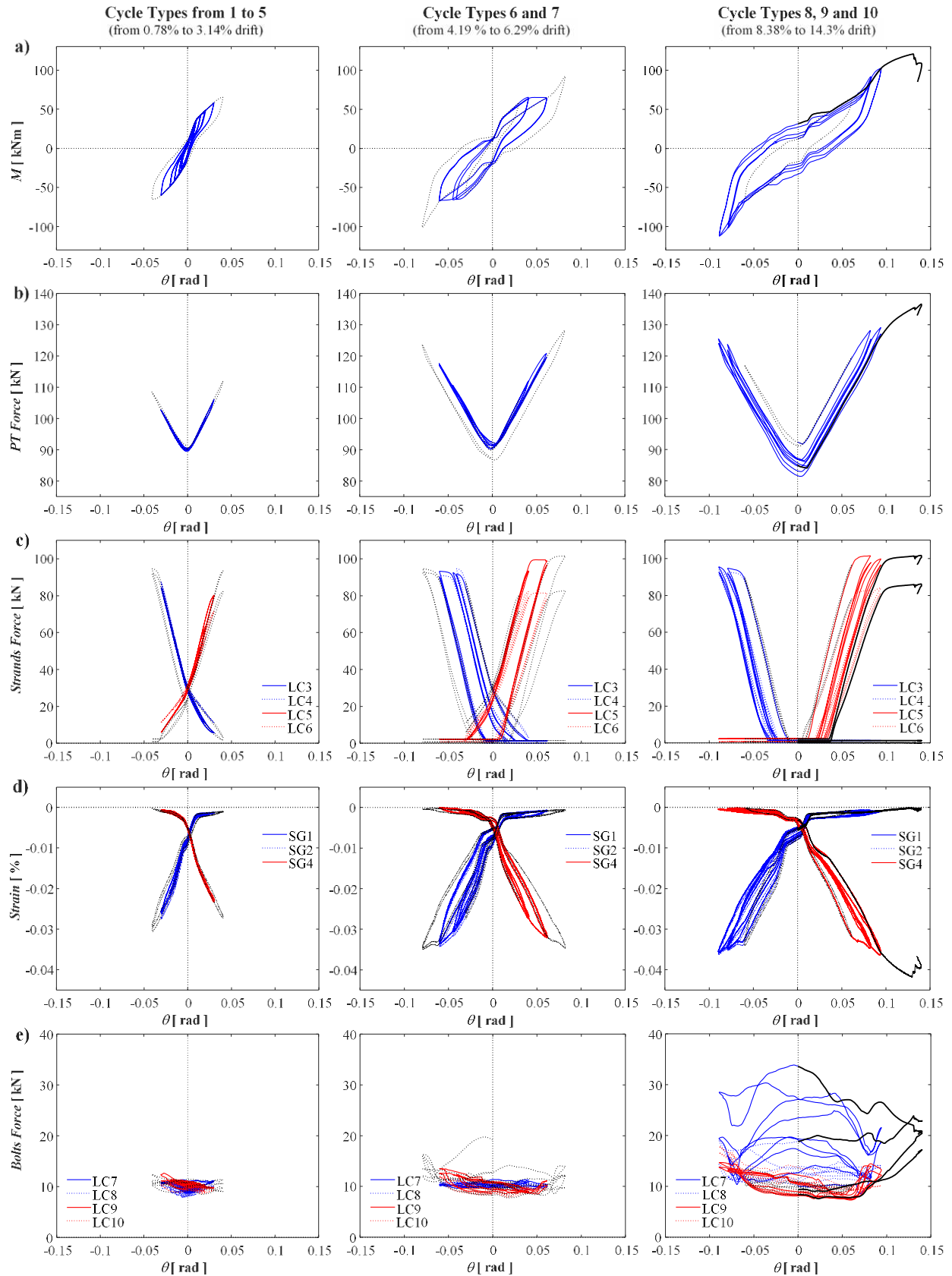


476 **Fig. 19.** Cyclic test for column type D. (a) Column rocking on the right edge with 0.095 rads (9.5 % drift) and (b)
 477 column rocking on the left edge with 0.143 rads (14.3 % drift)



478 **Fig. 20.** Moment-rotation curve of the cyclic test for column type D for (a) cycle types from 1 to 5 with displacements
 479 amplitudes up to 33 mm (0.0314 rads, 3.14 % drift); (b) cycle for the whole test

480



481
482 **Fig. 21.** Cyclic test for column type D. (a) Moment-rotation curve; (b) PT bars' tension force; (c) strands' tension
483 force; (d) strain gauges' records and (e) bolts' tension force

484 For cycle types 1 to 5 of Fig. 21, the results were similar as that shown in Fig. 18 and were previously described.

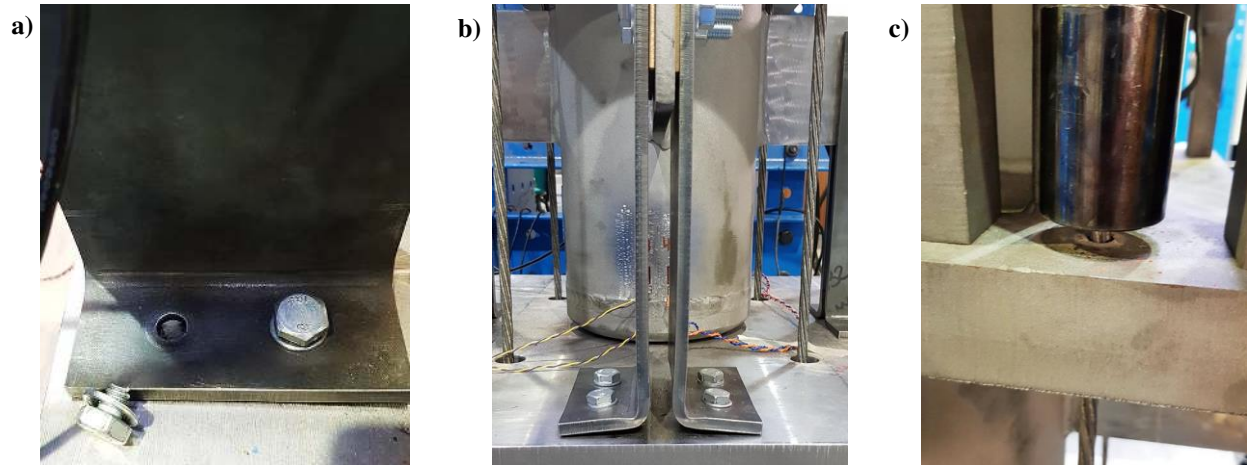
485 For cycle type 6, and 7, Fig. 21(c) shows the strands' yielding which resulted in an increase of deformation with a
486 nearly constant force. It is interesting to observe that the point when the first strands yielded, and the first loss of post-
487 tensioning force correspond to a rotation of about 0.03 rads, as expected from the design. As a consequence of the
488 yielding and of the residual elongation of the strands, their force corresponding to a zero rotation is equal to zero (*i.e.*,
489 loss of post-tensioning force) at the end of cycle type 7. This affected the moment-rotation curve, shown in Fig. 21(a),
490 where the post-elastic behavior exhibited low strain-hardening and reduction of the initial stiffness of the column base.
491 Fig. 21(d) shows small post-elastic behavior of the column base's hollow section, as described by the strain gauges
492 records. For these amplitudes there is no bearing of the FDs' bolts, as expected, based on the dimensions of the slotted
493 holes and there was a nearly constant bolt tension force as shown in Fig. 21(e).

494 For cycle types 8, 9, and 10, Fig. 21(a) shows a significant increase of the stiffness in the moment-rotation curve.
495 This is related to the bolts bearing, which was expected considering that the slotted holes of the FD were designed for
496 rotations up to 0.06 rads and as a consequence, Fig. 21(e) shows a significant increase of the longitudinal bolts' tension
497 force. Moreover, the increase of rotation amplitudes led to further yielding of the strands and of the hollow section
498 of the column base, as shown in Fig. 21(c) and (d). Additionally, Fig. 21(b) shows the behavior of the PT bars that, in
499 this case, experienced small plastic deformations and loss of PT force. However, this small reduction of the axial force
500 in the column do not significantly affect the final results of the experimental test.

501 The black solid lines, shown in the figures for cycle types 8, 9, and 10, show the final monotonic increase of
502 displacement leading to failure. Failure of one of the base bolts of the longitudinal FD in tension was observed for a
503 rotation of about 0.014 rads (14 % drift) as shown in Fig. 22(a).

504 Observation of the specimen after the final test allowed to identify the damaged components, *i.e.*, the strands and
505 the FDs undergoing plastic deformations. Fig. 22(a) and (b) show respectively the failure in the bolt and the residual
506 deformation in the base plates of the FD, while Fig. 22(c) shows the residual deformations in one strand. For
507 amplitudes within the target design rotation ($\theta_T = 0.03$ rads), the column base showed damage-free behavior, while
508 for very high rotations, even those significantly beyond the rotations of interest in earthquake engineering ($\theta \sim 0.14$),
509 the column base showed the ability to isolate damage in few easily replaceable components, demonstrating its high
510 potential to be used in highly earthquake-resilient steel structures.

511



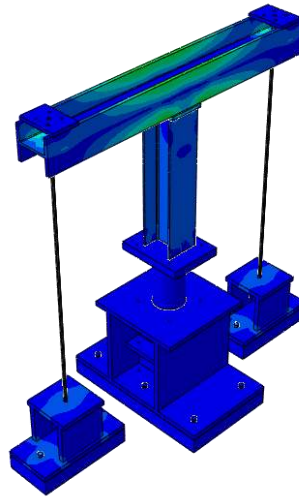
512 **Fig. 22.** Damage observed after the final cyclic test for column type D. (a) Failure of the FD's bolt; (b) residual
 513 deformations in the FDs' plates and (c) residual deformations in the strands

514 **9. NUMERICAL ANALYSIS**

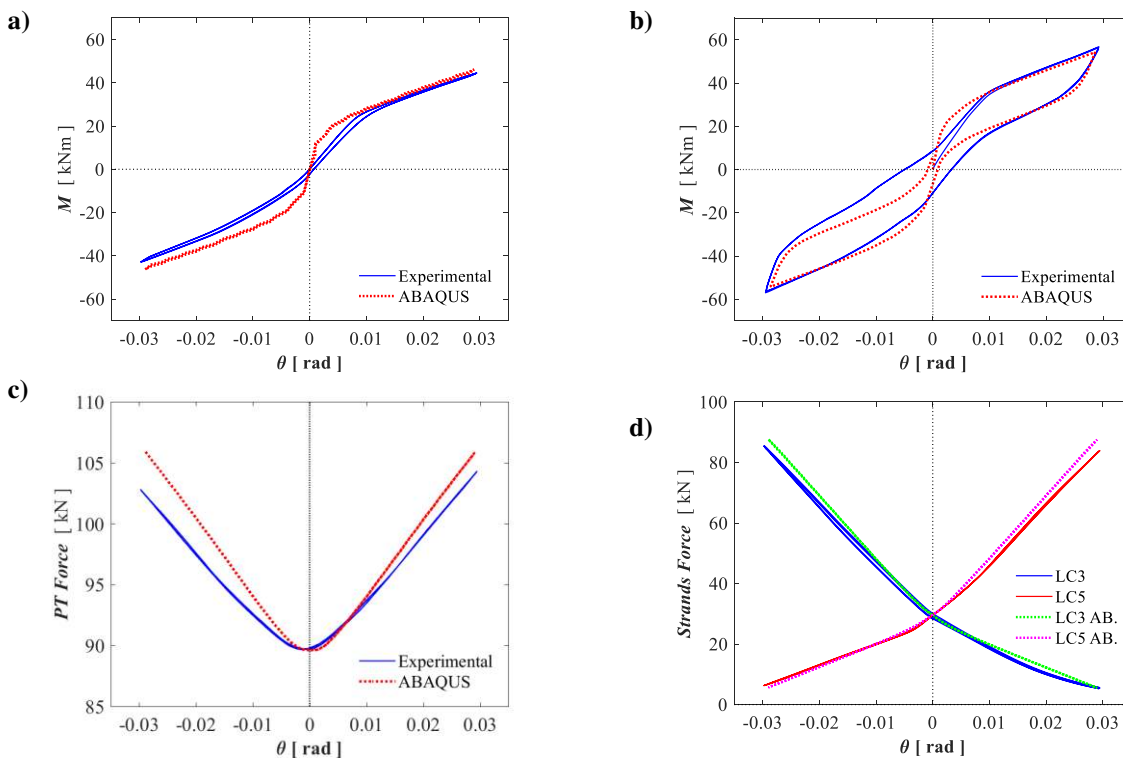
515 A detailed 3D numerical model of the column base was developed in ABAQUS (2013). All the components were
 516 modeled using the eight-node linear brick element, which relies on reduced integration and hourglass control, while
 517 meshing was carried out using the structured and swift mesh techniques. The multi-point constraint was used to
 518 simulate the weldings (*i.e.*, monolithic connection), while the contacts were modeled by the surface-to-surface
 519 interaction property. This was implemented by the no penetration contact condition for the behavior in the normal
 520 direction with the interface plane and by the penalty method for the tangential response. In the FDs the friction
 521 coefficient was defined based on the results of the characterization tests. The initial post-tensioning forces in bolts
 522 was modeled such as it remains constant throughout the analysis, differently, for the PT bars the post-tensioning force
 523 can varies according to the elongation or shortening during rocking. The nonlinear behavior of the materials was
 524 modeled by the von Mises yield criterion coupled with isotropic hardening by using the material properties obtained
 525 by the coupon tests. The static analysis procedure was used to solve the nonlinear equilibrium equations while the
 526 standard Newton solution technique was used for the application of the loads. Additional modeling details are provided
 527 in Freddi *et al* (2017).

528 The FE model in ABAQUS (2013) included the column base as well as the test setup components, as shown in Fig.
 529 23 in order to account for their deformability. Fig. 24 shows the comparison of the experimental and numerical results.
 530 It is worth noticing that, even before calibration, the ABAQUS model exhibited a quite accurate representation of the
 531 column base's behavior. Fig. 24(a) and (b) shows the moment-rotation curves of column base types B and D. Variation
 532 of the force in the PT bars and in the strands are shown, respectively in Fig. 24(c) and (d) for column base type B.
 533 Similar results were obtained for the other types, C and D.

534 The main difference between the numerical and experimental results is related to the reduced initial stiffness
 535 measured in the experimental tests and observed through comparison of the moment-rotation curves shown in Fig.
 536 24(a) and (b). This is often the case when comparing experimental and numerical results, and in the present case, this
 537 difference is mainly related to the imperfections in the coupling between the column base plate with the steel basement.



538 **Fig. 23.** Finite Element Model of the experimental test in ABAQUS (2013)
 539

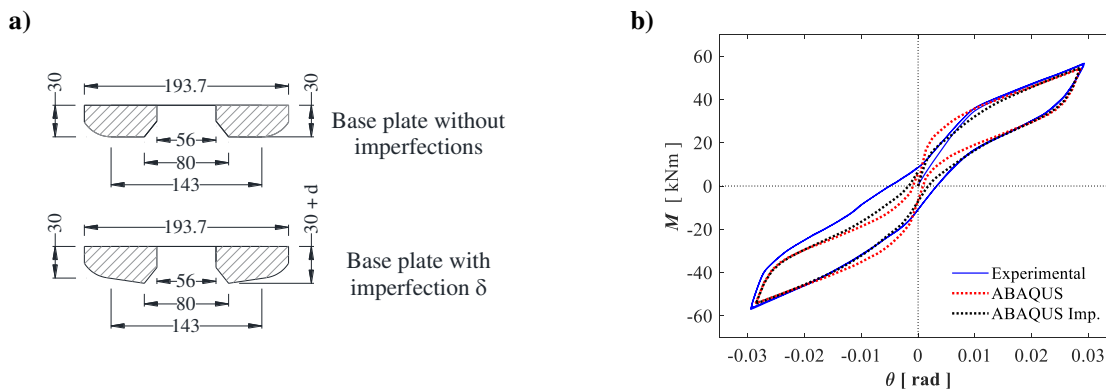


540 **Fig. 24.** Comparison between the experimental and numerical results in ABAQUS for the cyclic test up to the target
 541 rotation for: (a) Moment-rotation curve of column base type B; (b) Moment-rotation curve of column base type D.
 542 (c); PT bars tension force for the column base type B and (d) strands' tension force for the column base type B

543

544 Imperfections have been assessed according to the EN 1090-2 (2008) and included in the numerical ABAQUS models
 545 for the column base type D. The considered imperfection consisted of geometrical deviation in the plate with rounded
 546 edges and affected the contact conditions.

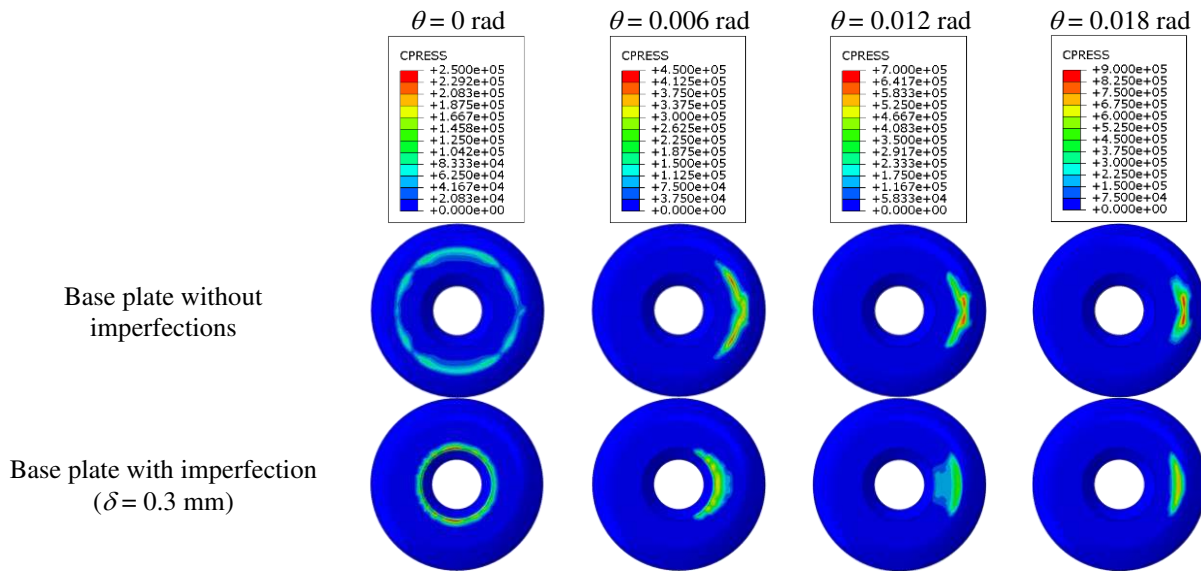
547 Without the imperfection, the central part of the steel plate with rounded edges is flat and in full contact with the
 548 steel basement. If the model account for these imperfections, the contact surface is limited before rocking. The local
 549 imperfection has been modeled as a symmetrical geometrical deviation as shown in Fig. 25(a).



550 **Fig. 25.** (a) Imperfections modelling: geometrical deviation in the plate with rounded edges; (b) Comparison between
 551 the experimental and numerical moment-rotation curves for the cyclic test up to the target rotation for the of column
 552 base type D. ABAQUS models with and without imperfections

553
 554 Several geometrical deviation amplitudes δ were investigated, *i.e.*, 0.3 mm, 0.7 mm, 1.0 mm and 1.4 mm and compared
 555 with the ‘perfect’ model ($\delta = 0.0$ mm). Fig. 25(b) shows, for the column type D, the comparison of the experimental
 556 results with the numerical results for the ‘perfect’ model and the model with a geometrical deviation with amplitude
 557 $\delta = 0.3$ mm. The comparison shows the impact that the imperfection can have on the initial stiffness without though
 558 affecting the moment-rotation response for rotations after the decompression.

559 Fig. 26 shows the comparison of the contact stresses for different rotation values of the column base with and
 560 without imperfections. It can be observed that the evolution of contact stresses is significantly different at the
 561 beginning of rocking, *i.e.*, the contact surface ‘moves quickly’ to the steel plate edge in the ‘perfect’ model while the
 562 transition requires a larger rotation in the case with imperfections. This influences the initial stiffness of the system.
 563 As a consequence of the imperfections, the distribution of stresses in the initial phase is significantly different, *i.e.*, at
 564 the end of post-tensioning of the PT bars and strands, the contact stresses are very localized in the imperfect models
 565 at the position where the imperfection amplitude is largest, while in the ‘perfect’ case, the contact stresses are
 566 distributed nearly uniformly over the whole surface of the steel plate.



567 **Fig. 26.** Contact stresses for different rotation values of column base with and without imperfections

568 The results show that the initial stiffness of the rocking system is significantly affected by this type of initial
 569 imperfection. Careful manufacturing process would allow a reduction of initial imperfection improving the confidence
 570 on the column base behavior. However, the results show that, even without considering the imperfections, the
 571 analytical formulation and the numerical model allow to capture the behavior of the column base after the
 572 decompression moment.

573 10. CONCLUSIONS

574 An earthquake-resilient rocking steel column base previously proposed and numerically investigated by the authors
 575 is experimentally tested. The proposed column base can be used to reduce residual deformations and damage in
 576 ‘innovative’ MRFs where the variations in the axial force associated with seismic overturning moment is limited. The
 577 column base uses post-tensioned (PT) high strength steel bars to control rocking behavior and friction devices (FDs)
 578 to dissipate seismic energy. A column base extracted from a prototype steel building was designed using a step-by-
 579 step design procedure, previously proposed by the authors, that aims to achieve damage-free and self-centering
 580 behavior for a predefined target rotation. Component tests for the characterization of the FDs were conducted to assess
 581 the relationship between the torque applied to high-strength bolts and the resistance (force corresponding to initiation
 582 of sliding) of the FDs. The experimental tests were conducted on a 3/5 scaled column base under monotonic and cyclic
 583 quasi-static lateral loading protocols while simulating an about constant axial force. The experimental results showed
 584 good agreement with the expected behavior from analytical equations, which validated the design procedure.

585 Moreover, they demonstrated the damage-free behavior up to the target design rotation and the ability to limit the
586 damage only to few easily replaceable components under large rotations. This demonstrates the high potential of the
587 innovative column base to be used in earthquake-resilient steel structures. The experimental results were also used to
588 calibrate refined 3D numerical models in ABAQUS that allowed to investigate the influence of the imperfections.
589 Amongst others, future research should focus on performing experimental dynamic tests to fully assess the seismic
590 performance of the proposed column base allowing the evaluation of the effect of the energy radiated during impact.
591 Moreover, additional research is required to reduce the uncertainty of the FDs response as consequence of the
592 variability of the bolt preload and the friction coefficient with time.

593 **DATA AVAILABILITY**

594 All data, models, or code generated or used during the study are available from the corresponding author by request.

595 **ACKNOWLEDGEMENTS**

596 This research is supported by Marie Skłodowska-Curie Action Fellowships within the H2020 European Programme.
597 Any opinions, findings, and conclusions or recommendations expressed in this paper are those of the authors and do
598 not necessarily reflect the views of the European Commission. The Authors also gratefully acknowledge the support
599 of Prof. J. Toby Mottram and the work of the technicians of the Structural Testing Laboratory of the University of
600 Warwick: Taylor Arnett and Neil Gillespie.

601 **REFERENCES**

- 602 ABAQUS/Standard and ABAQUS/Explicit – Version 6.13.1. ABAQUS Theory Manual, Dassault Systems, 2013.
- 603 Akcelyan, S., Lignos, D.G., Hikino, T., Nakashima, M. (2016). "Evaluation of Simplified and State-of-the-Art
604 Analysis Procedures for Steel Frame Buildings Equipped with Supplemental Damping Devices Based on E-
605 Defense Full-Scale Shake Table Tests." *J. Struct. Eng.*; **142**(6), 04016024.
- 606 ANSI/AISC 341-05. (2005) "Seismic Provisions for Structural Steel Buildings." *American Institute of Steel*
607 *Construction*, Chicago, Illinois.
- 608 Blomgren H-E., Pei, S., Jin, Z., Powers, J., Dolan, J.D., van de Lindt, J.W., Barbosa, A.R., Huang, D. (2019). "Full-
609 Scale Shake Table Testing of Cross-Laminated Timber Rocking Shear Walls with Replaceable Components." *J.*
610 *Struct. Eng.*; **145**(10), 04019115.
- 611 Borzouie, J., MacRae, G.A., Chase, J.G., Rodgers, G.W., Clifton, G.C. (2015). "Experimental studies on cyclic

612 performance of column base strong axis – aligned asymmetric friction connections.” *J. Struct. Eng.*; **142**(1),
613 04015078, 1–10.

614 BSI Standards Publication. (2012). "High tensile steel wire and strand for the prestressing of concrete - Specification".
615 *BS 5896:2012, The British Standards Institution, London, UK.*

616 Chi, H., Liu, J. (2012). “Seismic behavior of post-tensioned column base for steel self-centering moment resisting
617 frame.” *J. Constr. Steel Res.*, **78**, 117–130.

618 Chou, C-C., Chen, J.H. (2011). “Analytical model validation and influence of column bases for seismic responses of
619 steel post-tensioned self-centering MRF systems.” *Eng. Struct.*, **33**(9), 2628–2643.

620 Coelho, A., Bijlaard, F., Gresnigt, N., da Silva, L.S. (2004). “Experimental assessment of the behavior of bolted T-
621 stub connections made up of welded plates.” *J. Constr. Steel Res.*; **60**(2), 269–311.

622 CSI SAP2000. (2011). “Linear and Nonlinear Static and Dynamic Analysis and Design of Three-Dimensional
623 Structures: Basic Analysis Reference Manual”. *Computers and Structures, Inc. Berkeley, California.*

624 Dimopoulos, A.I., Tzimas, A.S., Karavasilis, T.L., Vamvatsikos, D. (2016). "Probabilistic economic seismic loss
625 estimation in steel buildings using post-tensioned moment-resisting frames and viscous dampers." *Earthquake*
626 *Eng. Struct. Dyn.*; **45**(11), 1725-1741.

627 Dimopoulos, C., Freddi, F., Karavasilis, T. (2019). “Progressive collapse resistance of steel self-centering MRFs
628 including the effects of the composite floor.” *Engineering Structures.*
629 <https://doi.org/10.1016/j.engstruct.2019.109923>

630 EN 1090-2. (2008) “Execution of steel structures and aluminum structures - Part 2: Technical requirements for steel
631 structures.” *European Committee for Standardization, Brussels, Belgium.*

632 EN 1991-1-1. (2001). “Eurocode 1: Actions on structures – Part 1-1: General actions – Densities, self-weight, imposed
633 loads for buildings.” *European Committee for Standardization, Brussels, Belgium.*

634 EN 1993-1-1. (2005). “Eurocode 3: Design of steel structures – Part 1-1: General rules and rules for buildings.”
635 *European Committee for Standardization, Brussels, Belgium.*

636 EN 1993-1-8. (2005). “Eurocode 3: Design of steel structures – Part 1-8: Design of Joints.” *European Committee for*
637 *Standardization, Brussels, Belgium.*

638 EN 1998-1-1. (2005). “Eurocode 8: Design of structures for earthquake resistance – Part 1: General rules, seismic
639 action and rules for buildings.” *European Committee for Standardization, Brussels, Belgium.*

640 EN ISO 6892-1. (2009) “Metallic materials - Tensile testing - Part 1: Method of test at room temperature.”
641 *European Committee for Standardization*, Brussels, Belgium.

642 Federal Emergency Management Agency (FEMA). (2000). “Recommended seismic design criteria for new steel
643 moment-frame buildings.” *FEMA 350, SAC Joint Venture*, Washington, DC.

644 Freddi, F., Tubaldi, E., Ragni, L., Dall’Asta, A. (2013). “Probabilistic performance assessment of low-ductility
645 reinforced concrete frame retrofitted with dissipative braces.” *Earthquake Eng. Struct. Dyn.*; **42**(7), 993–1011.

646 Freddi, F., Dimopoulos, C.A., Karavasilis, T.L. (2017). “Rocking damage-free steel column base with friction devices:
647 design procedure and numerical evaluation.” *Earthquake Eng. Struct. Dyn.*; **46**(14): 2281-2300. DOI:
648 10.1002/eqe.2904.

649 Garlock, M., Sause, R., Ricles, J.M. (2007). “Behavior and design of posttensioned steel frame systems.” *J. Struct.*
650 *Eng.*; **133**(3), 389–399.

651 Gioiella, L., Tubaldi, E., Gara, F., Dezi, L., Dall’Asta A. (2018). “Modal properties and seismic behaviour of buildings
652 equipped with external dissipative pinned rocking braced frames.” *Eng. Struct.*; **172**, 807–819.

653 Grauvilardell, J.E., Lee, D., Hajjar, J.F., Dexter, R.J. (2006). “Synthesis of design, testing and analysis research on
654 steel column base plate connections in high-seismic zones.” *Report ST-04-02*, Dept. of Civil Engineering, Univ.
655 of Minnesota, USA.

656 Grigorian, C.E., Yang, T.S., Popov, E.P. (1993). “Slotted bolted connection energy dissipators.” *Earthq. Spectra*; **9**(3):
657 491–504.

658 Haremza, C., Santiago, A., da Silva, L.S. (2013). “Experimental behavior of heated composite steel–concrete joints
659 subject to variable bending moments and axial forces.” *Eng. Struct.*; **51**, 150–161.

660 Ikenaga, M., Nagae, T., Nakashima, M., Suita, K. (2006). “Development of column bases having self-centering and
661 damping capability.” *5th Int. Conf. on Behaviour of Steel Structures in Seismic Areas*, Yokohama, Japan.

662 Kamperidis, V.C., Karavasilis, T.L., Vasdravellis, G. (2018). “Self-centering steel column base with metallic energy
663 dissipation devices.” *J. of Constr. Steel Res.*; **149**, 14–30.

664 Kanvinde, A.M., Grilli, D.A., Zareian, F. (2012). “Rotational stiffness of exposed column base connections:
665 experiments and analytical models.” *J. Struct. Eng.*; **138**(5), 549–560.

666 Kelly, J.M., Tsztoo, D.F. (1977). “Earthquake simulation testing of a stepping frame with energy-absorbing devices.
667 *NZ Soc. Earthquake Eng. Bull.*; **10**(4): 196-207.

668 Kim, H.J., Christopoulos, C. (2008). “Seismic design procedure and seismic response of post-tensioned self-centering

669 steel frames.” *Earthquake Eng. Struct. Dyn.*, **38**(3), 355–376.

670 Latour, M., Rizzano, G. (2013). “Full strength design of column base connections accounting for random material
671 variability.” *Eng. Struct.*; **48**, 458–471.

672 Latour, M., Rizzano, G. (2013). “A theoretical model for predicting the rotational capacity of steel base joints.” *Eng.*
673 *Struct.*; **91**, 89–99.

674 Latour, M., Piluso, V., Rizzano, G. (2015). “Free from damage beam-to-column joints: Testing and design of DST
675 connections with friction pads.” *Eng. Struct.*; **85**, 219–233.

676 Latour, M., Rizzano, G., Santiago, A., da Silva, L.S. (2019). “Experimental response of a low-yielding, re-centering,
677 rocking base plate joint with friction dampers.” *Soil Dyn. Earthq. Eng.*; **116**: 580-592.

678 Mackinven, H., MacRae, G.A., Pampanin, S., Clifton, G.C., Butterworth, J. (2007). “Generation four steel moment
679 frame joints.” *8th Pacific Conf. on Earthq. Eng.*, Singapore.

680 MacRae, G.A., Urmson, C.R., Walpole, W.R., Moss, P., Hyde, K., Clifton, C. (2009). “Axial shortening of steel
681 columns in buildings subjected to earthquakes.” *Bull. New Zeal. Soc. Earthq. Eng.*, **42**(4): 275–287.

682 McKenna, F., Fenves, G.L., Scott, M.H. (2006). “OpenSees: Open system for earthquake engineering simulation.”
683 *PEER Center*, Berkeley, CA. Wolski, M., Ricles, J., Sause, R. (2009). “Experimental Study of a Self-Centering
684 Beam–Column Connection with Bottom Flange Friction Device.” *J. Struct. Eng.*; **135**(5), 479–488.

685 Rodas, P.T., Zareian, F., Kanvinde, A. (2016). “Hysteretic model for exposed column-base connections.” *J. Struct.*
686 *Eng.*; **142**(12), 04016137, 1–14.

687 Symans, M.D., Charney, F.A., Whittaker, A.S., Constantinou, M.C., Kircher, C.A., Johnson, M.W., McNamara, R.J.
688 (2008). “Energy dissipation systems for seismic applications: Current practice and recent developments.” *J. Struct.*
689 *Eng.*; **134**(1), 3–21.

690 Takamatsu, T., Tamai, H. (2005). “Non-slip-type restoring force characteristics of an exposed-type column base.” *J.*
691 *Constr. Steel Res.* **61**(7): 942–961.

692 Tzimas, A.S., Kamaris, G.S., Karavasilis, T.L., Galasso, C. (2016). "Collapse risk and residual drift performance of
693 steel buildings using post-tensioned MRFs and viscous dampers in near-fault regions." *Bulletin Earthq. Eng.*;
694 **14**(6), 1643-1662.

695 Vasdravellis, G., Karavasilis, T.L., Uy, B. (2013). “Large-scale experimental validation of steel posttensioned
696 connections with web hourglass pins.” *J. Struct. Eng.*; **139**(6), 1033–1042.

697 Wang, X.T., Xie, C.D., Lin, L.H., Li, J. (2019). “Seismic behavior of self-centering concrete-filled square steel tubular

- 698 (CFST) column base.” *J. of Constr. Steel Res.*; 156: 75–85.
- 699 Yamanishi, T., Kasai, K., Takamatsu, T., Tamai, H. (2012). “Innovative column-base details capable of tuning rigidity
700 and strength for low to medium-rise steel structures.” *15th World Conf. on Earthq. Eng.*, Lisbon, Portugal.
- 701 Zareian, F., Kanvinde, A. (2013). “Effect of column-base flexibility on the seismic response and safety of steel
702 moment-resisting frames.” *Earthq. Spectra*; **29**(4), 1537–1559.